

Seventh National Image-Guided Therapy Workshop



September 18, 2014
Boston, MA

www.ncigt.org

Workshop Chairs

Tina Kapur, PhD
Ferenc Jolesz, MD
Clare Tempany, MD

Workshop Coordinator

Danielle Chamberlain, BS, RT(R)

Welcome

Welcome to the Seventh Image-Guided Therapy workshop sponsored by the US National Center for Image Guided Therapy (NCIGT, P41EB015898), the Neuroimage Analysis Center (P41EB015902), and two National Institutes of Health – the National Cancer Institute, and the National Institute for Biomedical Imaging and Biomedical Engineering.

The overall goal of this workshop series is to highlight the current needs and opportunities in the field of image-guided therapy and the role of NCIGT as a national center serving the greater IGT community.

The program for this Seventh workshop includes a single track of scientific talks that are grouped into sessions that share either a clinical focus--Brain, Endovascular, Pelvic, Abdominal, Skin--or a technology focus--Ultrasound, Robotics. The program also includes a poster session that spans these focus areas as well as Human Computer Interface for interventional workflows.

Similar to previous workshops in this series, we are honored to have in attendance our colleagues from academia, industry, as well as the National Institutes of Health. We hope that you continue to contribute to the success of this workshop by your participation.

Sincerely,

Workshop Chairs

ORAL PROGRAM
8:00 AM- 5:00 PM

7:00AM	Coffee and Breakfast	
8:00 AM	Welcome	Tina Kapur, PhD Brigham and Women's Hospital & Harvard Medical School
8:10-9:30 AM	SESSION ONE: BRAIN Session Chair: Michael Miga, PhD, Vanderbilt	
8:10 AM	Introduction to Session I	Michael Miga, PhD Vanderbilt
8:20 AM	1. Open-Source 3D Ultrasound Visualization for ease of Interpretation during Brain Tumor Resection	Alexandra Golby, MD Brigham and Women's Hospital & Harvard Medical School
8:32 AM	2. Sensitivity-Based Acquisition Model for Intra-Operative Positron Imaging in Neurosurgery	Frederic Monge, PhD Candidate Université de Rennes, France
8:44 AM	3. Importance of MR Imaging Feedback in the Administration of Therapeutics via Convection Enhanced Delivery	Alastair J. Martin, PhD University of California, San Francisco
8:56 AM	4. Preliminary predictions from an inverse problem-trained model	Samuel Fahrenholtz, PhD Candidate University of Texas MD Anderson Cancer Center
9:08 AM	5. Two-tensor Unscented Kalman Filter Tractography Offers Improved Corticospinal Tract Modeling by Resolving the Effects of Peritumoral Edema and Crossing Fibers	Lauren O'Donnell, PhD Brigham and Women's Hospital & Harvard Medical School
9: 0-11:00 AM	SESSION TWO: POSTERS AND COFFEE	
11AM-12:00 PM	SESSION THREE: ULTRASOUND Session Chair: David Hawkes, PhD, University College of London	
11:00 AM	Introduction to Session III	David Hawkes, PhD University College of London
11:10 AM	6. Real-time EM navigated breast conserving surgery: phantom and cadaver experiments	Gabor Fichtinger, PhD Queen's University, Kingston, ON, Canada
11:22 AM	7. Towards ProbeSight: Integration of a prior high-resolution 3D surface map into a probe-mounted camera system to locate the ultrasound probe relative to the patient	Jihang Wang, PhD Candidate University of Pittsburgh
11:34 AM	8. Bidimensional Localization of Active Ultrasound Markers	Guillaume Custillon, PhD Grenoble CIC-IT, France
11:46 AM	9. Automatic Recognition of the Target Plane in 3D Ultrasound with EpiGuide	Mehran Pesteie, PhD Candidate University of British Columbia, Vancouver, BC, Canada
12:00-1:00 PM	LUNCH	
1:00-2:00 PM	SESSION FOUR: ROBOTICS Session Chair: Junichi Tokuda, PhD, Brigham Women's Hospital & Harvard Medical School	
1:00 PM	Introduction to Session IV	Junichi Tokuda, PhD Brigham and Women's Hospital & Harvard Medical School
1:08 PM	10. Multisection Tendon-Driven Robot with Prismatic Joint for Neuroendoscopy	Nobuhiko Hata, PhD Brigham and Women's Hospital & Harvard Medical School

1:20 PM	11. MRI-Powered, imaged and controlled actuators for interventional robots	Ouajdi Felfoul, PhD Boston Children's Hospital & Harvard Medical School
1:32 PM	12. Real-Time Dynamic Scan Plane Control for Effective MRI-Guided Robotic Interventions	Mahamadou Diakite, PhD University of Maryland
1:44 PM	13. Fusion of laparoscopic ultrasound with MRI during robotically assisted nephrectomies	Samuel Kadoury, PhD Polytechnique Montreal
1:56-3:00 PM	SESSION FIVE: PELVIC, ABDOMINAL, SKIN Session Chair: Kristy Brock, PhD, University of Michigan	
1:56 PM	Introduction to Session V	Kristy Brock, PhD University of Michigan
2:04 PM	14. Lightfield 3D Endoscope for Minimally Invasive Surgery	Jason Geng, PhD Xigen LLC, Gaithersburg, MD
2:16 PM	15. Implementing Therapeutic Dose-Volume Liver Response in Biomechanical Modeling	Daniel Polan University of Michigan
2:28 PM	16. Oxygenation Assessment in Residual Gynecologic Cancers after External Beam Radiation: Preliminary Characterization using T2* Mapping	Pelin Aksit Ciris, PhD Brigham and Women's Hospital & Harvard Medical School
2:40 PM	17. Reflectance Confocal Microscopy to Guide Laser Ablation of Basal Cell Carcinomas	Heidy Sierra, PhD Memorial Sloan-Kettering Cancer Center
2:52 PM	18. In vivo Confirmation of THz Wound Edema Imaging for Burn Surgery Using MR	Neha Bajwa, MS University of California, Los Angeles
3:00-3:30 PM	COFFEE BREAK	
3:30-5:00 PM	SESSION SIX: ENDOVASCULAR Session Chair: Pelin Ciris, PhD, Brigham and Women's Hospital & Harvard Medical School	
3:30 PM	Introduction to Session VI	Pelin Ciris, PhD Brigham and Women's Hospital & Harvard Medical School
3:38 PM	19. Magnetically Assisted Remote-controlled Endovascular Catheter for Interventional MR Imaging: In Vitro Navigation at 1.5 T versus X-ray Fluoroscopy	Steven Hetts, MD University of California, San Francisco
3:50 PM	20. How New High-Resolution Detector Systems can have High Impact on Minimally Invasive Image-Guided Interventions	Stephen Rudin, PhD University at Buffalo, State University of New York
4:02 PM	21. Positive contrast spiral imaging of a nitinol guidewire	Adrienne E Campbell-Washburn, PhD National Heart, Lung and Blood Institute, National Institutes of Health, Bethesda, MD
4:14 PM	22. MRI-based computer models using T1-mapping for guiding electrophysiology interventions	Mihaela Pop, PhD Sunnybrook Research Institute, University of Toronto, Canada
4:26 PM	23. Vascular Repair by MR RF Coagulation	Ouri Cohen, PhD Massachusetts General Hospital & Harvard Medical School

POSTER PROGRAM
9:30 AM- 11:00 AM

Brain	1. Finite element based biomechanical analysis of cranial shapes for craniosynostosis surgical correction	Ricardo Ortiz, PhD, Kitware
	2. Tissue characterization and blurring identification in temporal lobe epilepsy	Luiz Otavio Murta Junior, PhD Brigham and Women's Hospital & University of Sao Paulo
	3. Mutual Information Registration of MRI for Neurosurgical Applications	Meysam Torabi, MSc., Visualase, Inc
	4. Low Intensity Focused Ultrasound Acoustic Characterization through Skull	Meghedi Babakhanian University of California, Los Angeles
Endovascular, Cardiac, Vasculature	5. Development and Validation of an Endovascular Chemotherapy Filter Device for Removing High-Dose Doxorubicin from the Blood: In Vivo Porcine Study	Steven Hetts, MD University of California, San Francisco
	6. Quantitative ultra-high resolution MR imaging using magnetic nanoparticles	Codi Gharagouzloo, Ph.D Candidate Northeastern University
	7. Water Relaxation Parameters and the State of Protein Coagulation in Vascular Repair by MR Coagulation	Ming Zhao, PhD Candidate University of Massachusetts Lowell & Massachusetts General Hospital
	8. Rapid Segmentation of the Median Nerve for a Video-Guided Ultrasound System	Jihang Wang, PhD Candidate, University of Pittsburgh
Eye	9. Assessment of In-vivo Corneal Hydration using Terahertz Imaging	Shijun Sung, PhD Candidate, University of California, Los Angeles
Human Computer Interface	10. Implementation of gesture control concepts for data accessibility in intraoperative settings	Franklin King, PhD Candidate Queen's University, Kingston, ON, Canada
	11. Usability Evaluation of a Touchless User Interface for 3D Slicer	Tobias Penzkofer, MD Brigham and Women's Hospital & Harvard Medical School
Skin	12. Feasibility of intraoperative imaging with reflectance confocal microscopy to potentially guide Mohs surgery	Eileen Flores, MPH Memorial Sloan Kettering Cancer Center
Pelvic	13. Electromagnetic Tracking for Catheter Path Reconstruction	Elodie Lugez, M.Sc. Queen's University, Kingston, ON, Canada
	14. Effect of Data Acquisition Speed and Technique on the Identification of Brachytherapy Source Positions with an Electromagnetic Tracker	Sarah M. Don MIT
	15. Bi-exponential diffusion analysis in normal prostate and prostate cancer: transition vs peripheral zone consideration	Thiele Kobus Brigham and Women's Hospital, & Radboudumc, Nijmegen, The Netherlands
	16. Quantitative and volumetric analysis of prostate cancer using mpMRI: a comparison of wholemount correlation versus routine histopathology report	Andriy Fedorov, PhD Brigham and Women's Hospital & Harvard Medical School
Robotics	17. Clinical Application of 4-DOF Needle Guiding Manipulator for MRI-guided Transperineal Prostate Biopsy	Junichi Tokuda, PhD Brigham and Women's Hospital & Harvard Medical School

Thoracic	18. Evaluation of Breast Tissue with Confocal Strip Mosaicking Microscopy: a potential platform for rapid pathology to guide surgery	Sanjee Abeytunge, MS Memorial Sloan-Kettering Cancer Center
	19. CT based Radiomics data predicts for nodal involvement and overall survival in Non Small Cell Lung Cancer	Thibaud Coroller, M.Sc. Dana Farber Cancer Institute & Harvard Medical School
	20. Comparative Study of Validation Metrics for Percutaenous Microwave Ablation against a 4D Thermal Simulation	Garron Deshazer, PhD Candidate University of Rhode Island
	21. Lung segmentation in 3D CT Images of Induced Acute Respiratory Distress Syndrome	Alfredo Morales Pinzón, PhD Candidate Universidad de los Andes, Bogotá, Colombia
Ultrasound Guidance	22. Advanced Approaches to Ultrasound Calibration: Planning a MICCAI Challenge	Emad Boctor, PhD Johns Hopkins Medical School

ABSTRACTS FOR ORAL PRESENTATIONS

Open-Source 3D Ultrasound Visualization for ease of Interpretation during Brain Tumor Resection

Alireza Mehrtash¹, Isaiah Norton¹, Parviz Dolati¹, Rahul Sastry¹, Andras Lasso²,
Matthew Toews¹, Tina Kapur¹, Steve Pieper³, William Wells III¹, Alexandra Golby¹

¹ Harvard Medical School, Brigham and Women's Hospital, Boston, MA ² Percutaneous Surgery Laboratory, School of Computing, Queen's University, Kingston, ON ³ Isomics, Inc., Cambridge MA

Purpose: Neuronavigation systems are widely used in routine neurosurgical interventions to provide real-time visualization of patient anatomy. These systems by design use pre-operative MR or CT image data which cannot reflect intraoperative brain tissue deformations including tissue resection which is particularly difficult to model. Ultrasound (US) provides a portable, inexpensive, fast and safe technology for acquiring serial image data in the course of surgery that could aid the characterization of brain tissue shifts. We propose an open-source technology to acquire and visualize 3D ultrasound image data alongside the pre-operative images in order to improve visualization and interpretation of the neuronavigation imaging data.

Method: In the Advanced Multimodality Image Guided Operating (AMIGO) suite in Brigham and Women's hospital, multiple ultrasound image acquisitions were performed at different time points of the image-guided craniotomy procedure: at post dural opening, in the course of resection and after total resection. The patient coordinate system was registered to the BrainLab neuronavigation image space. Temporal and spatial calibration of BK craniotomy ultrasound probe were performed with the Public Library for Ultrasound research (PLUS) before the procedure. The tracked US image data including image frames (acquired with Epiphan frame-grabber) and 6 DOF position and orientation of the US probe (from BrainLab) were sent to the visualization workstation through the openIGTLink network protocol. PlusServer application controlled through the SlicerIGT module inside 3D Slicer (<http://slicer.org>) was used to record 2D US images and create a 3D reconstruction of the recorded volume.

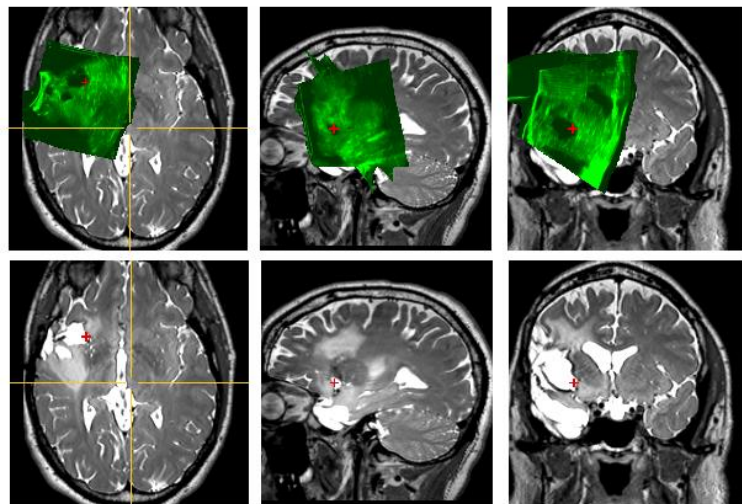


Figure 1: Top row: Updated neuronavigation visualization scene with the latest acquired 3D US volume rendered on the top of MR. Bottom row: Pre-operative MR image (The cavity at the left of axial view is from a previous resection)

PlusServer application controlled through the SlicerIGT module inside 3D Slicer (<http://slicer.org>) was used to record 2D US images and create a 3D reconstruction of the recorded volume.

Results: The proposed infrastructure recorded and reconstructed real-time 3D US on a standard PC computer with acceptable performance. Neuronavigation scene was updated according to the intraoperative ultrasound (Figure 1) and rendered on 3D Slicer alongside the BrainLab screen by thresholding and overlaying of the last reconstructed ultrasound volume.

Conclusion: Our research demonstrated the feasibility of fast and reliable serial intraoperative 3D ultrasound acquisition and visualization in image guided craniotomy.

Acknowledgements: This work is funded as part of the Neuroimaging Analysis Center (NAC), grant number P41EB015902, in collaboration with the National Center for Image Guided Therapy (NCIGT) grant number P41EB015898.

Sensitivity-Based Acquisition Model for Intra-Operative Positron Imaging in Neurosurgery

Frédéric Monge^{1,2}, Dzhoshkun I. Shakir³, Florence Le Jeune⁴, Xavier Morandi⁵, Nassir Navab³, and Pierre Jannin^{1,2}

¹ INSERM, UMR 1099, Rennes, F-35000, France

² LTSI, Campus de Villejean, Université de Rennes 1, Avenue Léon Bernard, Cedex 35043, Rennes, France

³ CAMP, Technische Universität München, Munich, Germany

⁴ Service de Médecine Nucléaire, Centre Eugène Marquis, Rennes, F-35000, France

⁵ CHU Rennes, service de Neurochirurgie, Rennes, F-35000, France

1 Purpose

Assisting surgeons in detecting residual tumor after resection is necessary for improving the survival prognosis of the patient. Towards that objective, freehand beta probes in conjunction with tracking systems (e.g. neuronavigation devices) and radiotracers like [¹⁸F]FET have shown a great potential. Nevertheless, beta probes' low spatial resolution makes it difficult to obtain sufficient tumor-to-background signal contrast. Acquisition models have been developed to reconstruct images from combined probe-tracking signal data, improving the accuracy of residual tumour border detection.

2 Methods

Based on an existing baseline ad-hoc model, we propose a new detection model within an integration of a customized sensitivity parameter designed for beta probes, estimated in optimal as well as intra-operative conditions. Since in-vivo testing is not an option yet, we evaluate the model with [¹⁸F] sources in realistically designed setups.

3 Results

We show significant improvements of the reconstructed signals in terms of spatial resolution, as well as the limits of the probe's detection capabilities, compared to the baseline. In numbers, we obtain a resolution of 3.8 mm on physical phantoms along one dimension, achieving an overall improvement of 20%.

4 Conclusion

Future work lies in assessing beta probe imaging using our new model on a realistic neurosurgical phantom, in terms of residual tumor topology and radiotracer uptake.

5 Funding sources

The authors thanks DAAD EGIDE-PROCOPE partners for French-Bavaria student exchanges and DFG SFB 824 for material support.

Importance of MR Imaging Feedback in the Administration of Therapeutics via Convection Enhanced Delivery

Alastair J. Martin ¹, Krystof Bankiewicz ², John Bringas ², Chadwick Christine ³, Paul S. Larson ²,
Departments of Radiology ¹, Neurological Surgery ², and Neurology ³, UCSF

Purpose: Convection enhanced delivery (CED) is a promising approach for delivering therapeutics to the brain. It bypasses the blood brain barrier and permits volumetric coverage of targeted brain structures. Prior clinical trials that have utilized CED to administer therapeutics have produced sub-standard outcomes and technical limitations in the administration of the therapy are considered to be a significant contributing factor to these failures. We are performing a phase I safety study that utilizes an optimized delivery platform and MR guidance to administer a promising gene therapy agent (AAV2-hAADC) in patients with Parkinson's disease. The aim of this study was to evaluate the use of imaging feedback to determine whether CED infusions are achieving their desired target coverage.

Methods: All patients were consented under a protocol approved by our institutional committee on human research. Patients were brought to the MR suite and underwent MR imaging to delineate the putamen and select preferred infusion sites. A burrhole was created at the desired entry site and an MR compatible trajectory guide (ClearPoint, MRI Interventions, Irvine, CA) affixed to the skull. The trajectory guide was oriented under real-time imaging to be directed to the selected targets within the putamen and a 16-gauge stepped infusion cannula inserted. The vector solution was mixed with an MR contrast agent (Prohance to 1mM final) to enhance CED infused regions and a ramped infusion rate paradigm was employed. At each new cannula location infusion rates began at 1 μ l/min and were ramped up as high as 10 μ l/min. Continuous MP-RAGE imaging with isotropic 1mm voxels was performed to monitor the infusion.

Results: All patients successfully underwent bilateral infusion of the putamen. In order to improve coverage anterior and posterior infusions were performed for a total of four infusions per patient. CED infusion progress was successfully monitored with MR imaging and several factors that led to non-ideal CED infusions were identified. The stepped cannula limited backflow but this remains a challenge for CED infusions (Figure 1). Surrounding anatomical structures, including vascular and CSF spaces also could lead to non-ideal coverage of the putamen (Figure 2). Detection of non-ideal CED infusions permitted real time adjustment to infusion strategy, including changing cannula depth and aborting ineffective infusions.

Conclusions: CED administration into the putamen of Parkinson's patients frequently deviates from the intended coverage. Real time imaging feedback is crucial to detect when non-ideal coverage occurs in order to allow for corrective measures or the termination of an ineffective infusion.

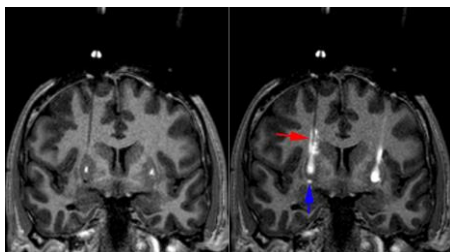


Figure 1: Bilateral infusion of the putamen is shown in coronal planes at the start of infusion (left) and near completion (right). Evidence of reflux is evident, especially on the right.

Funding Sources:
Michael J Fox
Clinical Intervention
Award

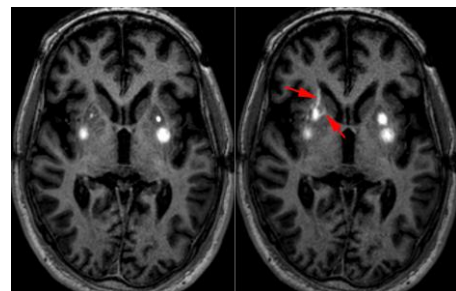


Figure 2: Bilateral infusion of the putamen is shown in axial planes at the start of anterior infusions (left) and near completion (right). Shunting via vascular channels can be appreciated on the subject's right side (arrows)

Title: Preliminary predictions from an inverse problem-trained model

Authors: SJ Fahrenholtz^{1,2}, RJ Stafford^{1,2}, JD Hazle^{1,2}, Anil Shetty³, D Fuentes^{1,2}

Affiliations: **1**— University of Texas MD Anderson Cancer Center; **2**— University of Texas at Houston, Graduate School of Biomedical Sciences; **3**— Visualase, Inc, Houston, TX

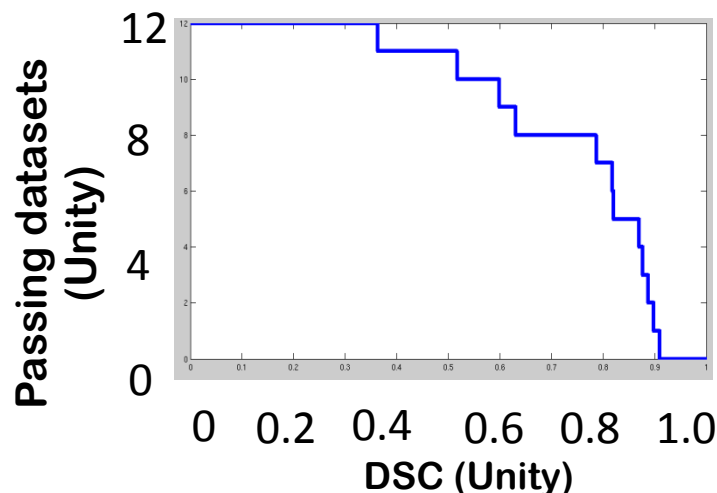
Purpose: MR-guided laser induced thermal therapy (MRgLITT) is a minimally invasive intervention showing promise in treatment of intracranial lesions. MRgLITT in brain stands to benefit from a computational model that can predict the largest ablation size, aiding in the planning of laser fiber placement. In this investigation, a steady-state Green's function solution to the Pennes bioheat equation is trained on retrospective brain MR temperature imaging (MRTI). Then, the trained model's predictive value is evaluated via leave-one-out cross validation.

Methods: There are conceptually three parts to the methods: model training, identification of MRTI datasets for which the model is appropriate, and evaluating the trained model's predictive value among appropriate datasets. For 33 MRTI datasets, a rectangular region of interest (ROI) manually highlighted the heated region. The hottest time point was found by summing the pixel-wise temperature values within the ROI and identifying the time point with the maximum temperature sum. For each MRTI dataset, the steady-state Green's function (SSGF) solution's optimal effective optical attenuation coefficient, μ_{eff} , was found via an inverse problem. The optimal μ_{eff} was determined by maximizing the Dice similarity coefficient (DSC) between the 57 °C isotherms of the MRTI and SSGF prediction. Datasets with optimal DSC > 0.8 were considered to have SSGF solutions that were appropriate for the dataset. Among these passing datasets, the predictive performance was quantified by DSC in a leave-one-out cross validation scheme.

Results: 12 MRTI datasets had optimal DSC > 0.8. For the 12, the μ_{eff} mean was 3176 m⁻¹. Leave-one-out cross validation was performed among these 12, producing the results in Figure 1. The DSC mean was 0.748, median was 0.819, and the standard deviation was 0.178. Eight datasets pass DSC > 0.7.

Conclusions: The trained model has some predictive value; however, two primary improvements need to be implemented. First, the SSGF model is non-physical. While it is possible for the non-physical model to predict after training, a physical model can be regression tested with other vetted, boosting confidence in its performance. Second, a new method is required for identifying eligible MRTI datasets for the leave-one-out cross validation. Presently, the method is self-selective for datasets apt to give predictive results.

Funding Sources: We acknowledge NIH grants 5T32CA119930-03, 1R21EB010196-01, CA016672, and TL1TR000369.



Two-tensor Unscented Kalman Filter Tractography Offers Improved Corticospinal Tract Modeling by Resolving the Effects of Peritumoral Edema and Crossing Fibers

Zhenrui Chen^{1,4}, MD, PhD, Lauren O'Donnell^{1,2}, PhD, Yanmei Tie¹, PhD, Alireza Mehrdash^{1,2}, MS, Olutayo Olubiyi¹, MBChB, MPH, Laura Rigolo¹, MA, Isaiah Norton^{1,2}, BS, Ofer Pasternak³, PhD, Yogesh Rathi³, PhD, Alexandra J. Golby^{1,2}, MD

¹Departments of Neurosurgery, ²Radiology, and ³Psychiatry, Brigham and Women's Hospital, Harvard Medical School, Boston, MA, USA

⁴Department of Neurosurgery, Jinling Hospital, Southern Medical University (Guangzhou), Nanjing, Jiangsu, China.

Purpose: Both peritumoral edema and crossing fibers pose a major challenge to the corticospinal tract (CST) modeling in malignant brain tumor patients when using the conventional single-tensor streamline fiber tracking method. The aim of this study is to present a novel technique using a two-tensor unscented Kalman filter (UKF) that resolves the effects of peritumoral edema and crossing fibers in tracing the CST.

Methods: Four patients with malignant brain tumors in the vicinity of motor cortex underwent pre-surgical 3-Tesla magnetic resonance imaging including a diffusion-weighted sequence with 31 gradient direction. Fiber tracking was performed to delineate the CST using both single-tensor streamline and two-tensor UKF tractography techniques^[1,2], based on a two-regions-of-interest approach. The two-tensor UKF tractography was designed using a mixture of two Gaussian tensors. The model parameters were estimated using UKF and subsequently propagated in the most consistent direction. Results from the two techniques were compared side-by-side.

Results: The two-tensor UKF tractography could fully delineate the CST, whereas the CST displayed by single-tensor streamline tractography were incomplete or disrupted (Figure).

Conclusions: These findings suggest that two-tensor UKF tractography is able to trace the CST more accurately than single-tensor streamline tractography in the settings of peritumoral edema and crossing fibers. Two-tensor UKF tractography may be helpful in the quest to preserve motor function in brain surgery.

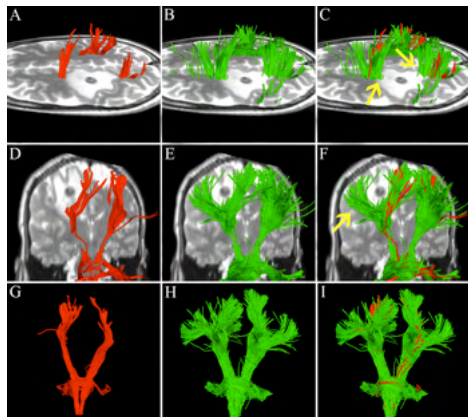


Figure. Comparison between CST tracking of patient 1 using single-tensor streamline (A and D, red) and two-tensor UKF tractography (B and E, green) methods. Compared with single-tensor streamline, two-tensor UKF tractography could delineate the CST portion that runs through peritumoral edema (C, yellow arrows), and the lateral branches of CST (F, yellow arrow), (G) and (H) show a side-by-side comparison of the entire CST, and (I) is an overlay view.

Acknowledgements

This work is supported by R21NS075728, P41EB015898, P41RR019703, and P01CA067165 and Oversea Study Program of Guangzhou Elite Project.

References

- [1] Malcolm, J. G., Shenton, M. E., & Rathi, Y. (2010). Filtered multitensor tractography. *Medical Imaging, IEEE Transactions on*, 29(9), 1664-1675.
- [2] O'Donnell, L.J., Cui, J.L., Marianayagam, N. et al. (2013). Single vs. multiple tensor diffusion tractography: which is better correlated with function? *Proceedings of the Sixth National Image Guided Therapy Workshop, Arlington, VA*. p. 40.

Real-time EM navigated breast conserving surgery: phantom and cadaver experiments

G. Gauvin¹, C.T. Yeo², T. Ungi², G. Fichtinger², S. Nanji¹, J. Rudan¹, C.J. Engel¹

¹Department of Surgery, Queen's University, CJay.Engel@krcc.on.ca

²School of Computing, Queen's University

Purpose

Breast cancer is ideally treated by breast-conserving surgery during its early stages. Current strategies, including gold-standard wire-localization, have positive margin rates as high as 47%. Positive margins are linked with a higher local recurrence rate. We propose real-time electromagnetic (EM) navigation system to improve the precision of the resection.

Methods

The proposed method builds on the current gold-standard method of wire-localization. One EM sensor is attached externally to the patient to create a global frame of reference, and one EM sensor is attached to the wire-localization needle to account for local deformation and movement of the breast tissue. An EM-tracked ultrasound (US) probe is used to register the tumor location and delineate the desired resection volume through the placement of 6 fiducial points and a surface model. A final sensor is attached to the cautery device to allow real-time visualization relative to the planned resection volume. Figure 1 illustrates the overall navigation system. We used a SonixGPS Tablet (Ultrasonix, Vancouver, CA) ultrasound with its built-in EM tracker. The scanner and tracker broadcast their data through the PLUS (www.plustoolkit.org) toolkit to the SlicerIGT navigation software (www.SlicerIGT.org), providing real-time visualization of the resection volume and cautery position with respect to the tumor.

Ten surgeons were recruited to resect non-visible, non-palpable tumors implanted in synthetic breast models. Each participant resected an equal number of tumors using the wire-localization method (control group n=21) and the EM navigation method (EM group

n=21). A cadaver study verified workflow feasibility on real breast tissue.

Results

The resected volumes were analyzed for presence of tumor at the edge of resection, size and weight of the resected volume. The positive margin rate in the control group was 42.9%, and the positive margin rate in the EM navigation group was 19.0% (p=0.18). The relative amount of tissue resected with each method was similar (36.3±14.5 control group vs. 37.7±9.8; p=0.87).

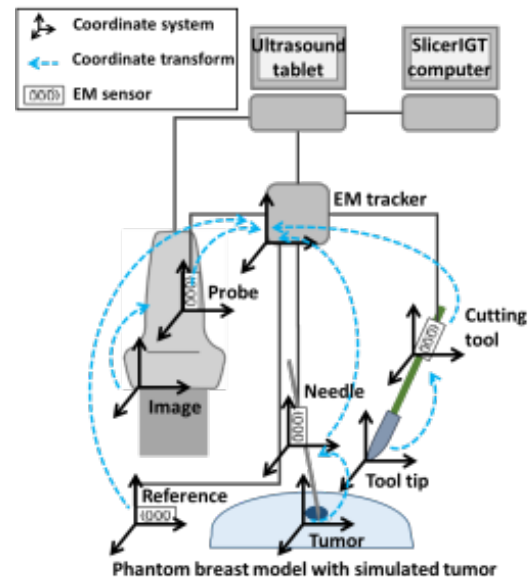


Fig 1. EM navigation system setup.

Conclusions

In a synthetic breast model, EM navigation reduces the positive margin rate without altering the amount of breast tissue removed. This proof of concept study demonstrates that navigation in breast-conserving surgery may improve treatment outcome.

Towards ProbeSight: Integration of a prior high-resolution 3D surface map into a probe-mounted camera system to locate the ultrasound probe relative to the patient

Jihang Wang¹, Samantha Horvath², John Galiotti^{1,3}, Vijay Gorantla², George Stetten^{1,3}

Departments of Bioengineering¹ and Reconstructive Surgery², University of Pittsburgh
Robotics Institute, Carnegie Mellon University³

Purpose

We are developing techniques for guidance of ultrasound probes with respect to the exterior of the patient using a video camera mounted on the probe. This method will permit the reconstruction of 3D ultrasound data as the probe is moved, as well as the comparison of a real-time ultrasound scan with previous scans from the same anatomical location, all without using external tracking devices.

Methods

Our embodiment of this concept involves three parts: acquisition of a high-resolution multi-camera surface map, projecting the surface map to simulate various camera views, and 2D matching between the projected surface map and actual the camera image. First, a preoperative scan is acquired using a Vectra multi-camera system to yield the 3D shape and high-resolution appearance of the external anatomy. For our initial experiments, we used a textured phantom, in the form of a model dinosaur, instead of a real patient. One video camera was mounted directly on the probe to display a real-time image during the scan. The 3D surface map was then properly rendered to simulate the 2D image that would be seen by the camera from a particular point of view. The actual optics of the camera has been modeled, including focal length, lens distortion, and location of entrance pupil. Finally, given a metric for matching the rendering of the surface map to the real-time camera image, we can find the best match among all possible camera viewpoints, so that the current probe's pose can be determined relative to the anatomy. We used a *normalized mutual information* (NMI) metric for the image matching process, which is better suited than normalized correlation for our purposes, since it can accommodate differences in background without prior segmentation.

Results

We used external optical tracking (Micron) to predict the projection of the surface map that would correctly match the actual image from the camera. Using this ground truth, we tested the accuracy of our image matching procedure by deviating along each of the six degree of freedom (DOFs) from the correct viewpoint, projecting the surface map from each new viewpoint, and computing the NMI metric between it and the actual camera image. Along each DOF, the NMI metric showed a clear maximum at the ground truth viewpoint.

Conclusion

With the present results, we have only demonstrated the accuracy of our projection method and the specificity of our matching process. In real applications, the challenge of efficiently searching the 6-DOF space for the correct image will need to be addressed, since this space is very large. We are currently using an inertial navigation system mounted on the probe to reduce the search space, based on orientation and linear acceleration from one video frame to the next. The major contribution described in this abstract is the use of a previously acquired high-resolution 3D surface map, against which a real-time camera image can be matched, to provide anatomical coordinates for an ultrasound probe or surgical tool to which the camera is mounted. We foresee the use of such systems having broad clinical impact on diagnostic and interventional procedures.

Bidimensional Localization of Active Ultrasound Markers

Guillaume Custillon¹, Sandrine Voros², Philippe Cinquin², An Nguyen-Dinh³, and Alexandre Moreau-Gaudry²

¹UJF-Grenoble 1, INSERM CIT803, CHU de Grenoble, France

²UJF-Grenoble 1, CNRS, INSERM CIT083, TIMC-IMAG, UMR 5525, Grenoble, France

³VERMON, 180 rue Général Renault, BP3813, 37038 Tours Cedex, France

Purpose

During laparoscopic surgeries, the structures targeted by the surgical intervention appear as the surgeon goes along the dissection and can be hidden beneath organs surfaces. Such “hidden” structures can be visualized thanks to the ultrasound (US) modality. Fusing the laparoscopic and ultrasound modalities during a laparoscopy could help the surgeon in the intra-operative planning of his surgical intervention, by improving the visualization of interesting structures.

Such a fusion is based on the ability to identify reference points in both modalities, which is very challenging. To facilitate this identification, we focus in this paper on presenting an innovative ultrasound marker that can be localized with respect to a custom-designed trans-urethral ultrasound probe.

Methods

We used an Ultrasonix SonixTouch ultrasound scanner. The main advantage of this system is its ability to design custom applications where all the parameters of the piezoelements of a probe can be controlled. This machine is used to control an innovative trans-urethral ultrasound probe, composed of 124 elements, and working at a central frequency of 7.66 MHz. The active marker is a small cylinder of 5 mm in height and 5 mm in diameter, containing a piezoelectric monoelement of 200 μm diameter. The central frequency of the marker is 5 MHz, and its field of emission is a 60° cone. Used as a pure acoustic transmitter, its isotropic behavior makes it suitable for localization, whatever its position relative to the probe.

The marker is used as a “pure acoustic transmitter”, and the probe as a “pure acoustic receiver”. The localization of the marker is based on the measure of the time of flight of the US signal between the marker and the probe. This technique, known as trilateration, is similar to the GPS localization.



Results

Experiment was carried out to demonstrate the feasibility of the marker localization in a phantom environment. We obtained an average RMS localization error of $232 \mu\text{m} \pm 127 \mu\text{m}$ on the whole measure set (60 measurements).

This experiment demonstrates the possibility to localize an active ultrasound marker in two dimensions in ideal conditions, ie when the marker faces the probe.

Conclusions

The main advantages of the innovative marker used in this work are: 1) the fact that it allows a decoupling of the marker’s localization and the imaging of the scene (the marker’s signal doesn’t pollute the image and vice-versa) 2) is its capacity to emit ultrasound waves over a large section of space (60°). The size of the markers make them compatible with laparoscopic surgery since they can be inserted through trocars.

In future work, with a motorized ultrasound probe, we should be able to localize several markers in three dimensions. 3D localization will enable these markers to be used as identifiable points in ultrasound and video imagery, allowing the virtual reconstruction of the prostate by augmented reality.

Automatic Recognition of the Target Plane in 3D Ultrasound with EpiGuide

Mehran Pesteie¹, Purang Abolmaesumi¹, Hussam Al-Deen Ashab¹, Vickie Lessoway², Simon Massey², Vit Gunka², Robert Rohling¹

¹ Department of Electrical and Computer Engineering, University of British Columbia, Vancouver, Canada

² BC Women's Hospital, University of British Columbia, Vancouver, Canada

Purpose: Lumbar epidural needle placement is a challenging anesthetic technique. There is growing interest in using ultrasound imaging for guidance. EpiGuide is a novel 3D ultrasound guidance system that can visualize the wave-like laminae of the vertebrae and identify the optimal needle insertion point.¹ However, the complex spinal anatomy with different wave-like structures, compounded by US noise, makes the accurate identification of appropriate plane difficult. The aim of this study is to propose an automated system that can identify precisely the optimal plane for epidural needle placement.

Methods: 104 volumes were acquired from 13 volunteers using a SonixTOUCH ultrasound machine (Ultrasonix Medical, Richmond, Canada) equipped with a 5 MHz 3D transducer placed within 10 mm of the midline and slightly angled by 5° - 10°. All of the planes of the volumes were labeled by a sonographer as either an optimal paramedian plane, which includes the laminae, or a non-optimal plane for epidural needle placement. Because of the wave-like appearance of the laminae, a directional feature extraction scheme would be beneficial for detecting the laminae among other spinal structures. We used the Sequency Ordered Hadamard Transform to extract features which are able to discriminate the horizontal, vertical and diagonal structures in different regions of the US image. Later, a two layer feed-forward neural network was trained based on the target labels provided by the sonographer for classification.

Results: The proposed method successfully classified the laminae and non laminae planes in 1031 images out of 1090 (95% accuracy). The sensitivity and specificity of our method is 93% and 97% respectively. Our proposed algorithm detected the laminae planes in 527 images out of 545, which shows that the precision of our method is 97%. Table 1 illustrates different spinal structures, namely spinous processes, laminae, facet joints and transverse processes and also normalized scores of the trained neural network for each of them respectively. As shown in Table 1, the laminae plane has a relatively higher score comparing to the other planes. We also validated our method by leaving one volunteer out, training the neural network for the rest of the volunteers and performing classification for the left-out volunteer. We repeated this procedure for all of the volunteers. The average accuracy was 94%.

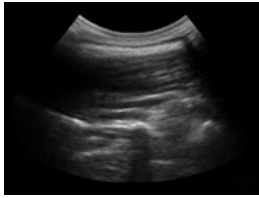
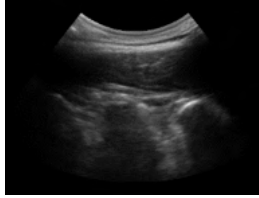
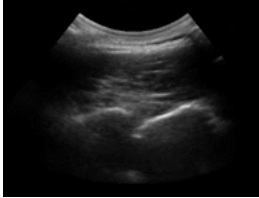
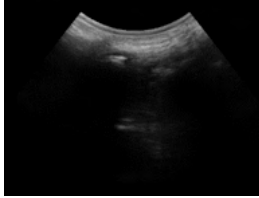
Transverse Processes	Facet joints	Lamina	Spinous Processes
			
Score = 0.25	Score = 0.19	Score = 0.79	Score = 0.00

Table 1. Different spinal structures and respective normalized scores

Conclusion: A machine learning algorithm based on regional features extracted by the Sequency Ordered Hadamard transform for detecting the laminae in ultrasound images has been proposed. The algorithm assists the anesthesiologist in finding the target for epidural needle placement with EpiGuide.

[1] P-A. Malenfant, V. Gunka, P. Beigi, A. Rasoulian, R. Rohling, A. Dube. Accuracy of 3D ultrasound for identification of epidural needle skin insertion point in parturients; a prospective observational study. Society for Obstetric Anesthesia and Perinatology (SOAP) 46th Annual Meeting, Toronto, ON, 2014.

Multisection Tendon-Driven Robot with Prismatic Joint for Neuroendoscopy

Takahisa Kato^{1,2}, Ichiro Okumura³, Hidekazu Kose³, Kiyoshi Takagi³, and Nobuhiko Hata¹
¹ National Center for Image Guided Therapy, Brigham and Women's Hospital and Harvard Medical School, MA, USA

² Healthcare Optics Research Laboratory, Canon U.S.A., Inc., MA, USA

³ Mechanics R&D Center, Canon Inc., Japan

Purpose: The purpose of this paper is to develop a tendon-driven robot by adding the multisection mechanism and a prismatic joint, and investigate the feasibility of using the robot to aim a neuroendoscope accurately but with more perspective than without the robot. The combination of the multiple sections and the prismatic joint allows full control of the position and direction of the endoscopic view with minimum cascaded multisection.

Methods: We developed a novel multisection tendon-driven robot with a prismatic joint to aim neuroendoscopes to planned position and direction (Figure 1). With the addition of the prismatic joint, the robot can position its tip along a planned trajectory or maintain gaze to a disease lesion. We newly developed an inverse kinematic mapping (IKM) considering the tendon friction of the multisection tendon-driven robot for improved control accuracy. We evaluated the tip control accuracy for the position and the direction along two functional trajectories, which are approach observation in a neuroendoscopic deep-brain surgery and circular observation around a deep-brain lesion.

Results: The results from this accuracy assessment indicated that the robot was operated at the mean accuracy of 6.1 mm for the position and 5.8 degrees for the direction. (Figure 2)

Conclusions: This paper presented a novel approach to aim endoscopes at controlled directions and positions using multisection tendon-driven robot with a prismatic joint. We also introduced the novel IKM to compute actuator parameters with the tension propagation model. We have also shown that our approach has the advantage to increase the end effector mobility of the endoscopes.

Funding Sources: Research reported in this publication was in part supported by CanonUSA, Inc, and The National Institute of Biomedical Imaging and Bioengineering of the National Institutes of Health under award number P41EB015898.

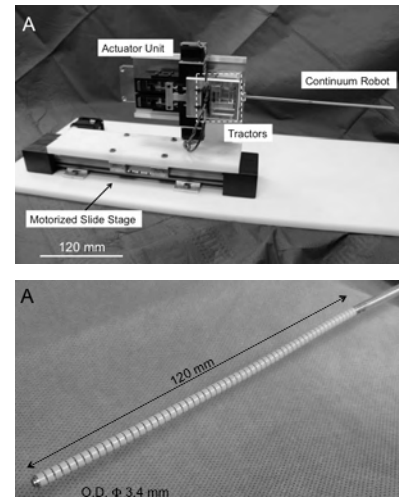


Figure 1. Two-section continuum robot with prismatic joint. (Top) Perspective view of the robot. (Bottom) Enlarged View of the two-section continuum robot.

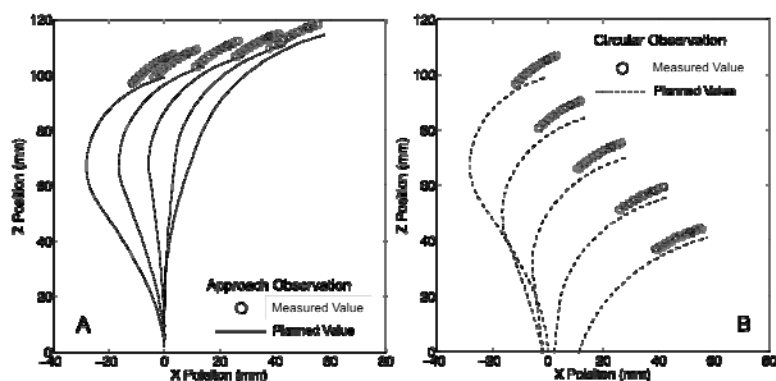


Figure 2. (Left-A) The result of approach observation. (Right B) result of circular observation. The commanded (lines) and measured (circles) postures were plotted.

MRI-Powered, imaged and controlled actuators for interventional robots

Ouajdi Felfoul¹, Aaron Becker¹, Pierre E. Dupont¹

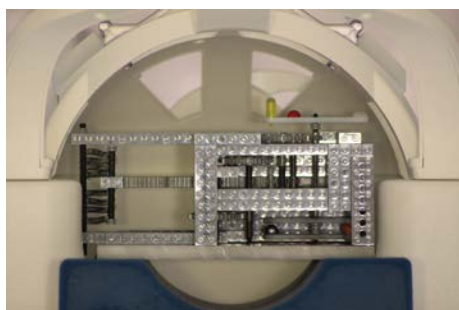
¹ Department of Cardiovascular Surgery, Boston Children's Hospital, Harvard Medical School, Boston, MA 02115 USA.

Purpose: Actuators that are powered, imaged and controlled by Magnetic Resonance (MR) scanners could inexpensively provide wireless control of MR-guided robots¹. Similar to traditional electric motors, the MR scanner acts as the stator and generates propulsive torques on an actuator rotor containing one or more ferrous particles. Generating maximum motor torque while avoiding instabilities and slippage requires closed-loop control of the electromagnetic field gradients, i.e., *commutation*. This abstract proposes and demonstrates a method for closed-loop commutation by interleaving pulse sequences for rotor imaging and rotor propulsion. Closed-loop commutation control using state-estimation increases motor torque, eliminates slippage, increases speed, and enables regulation of rotor angle.

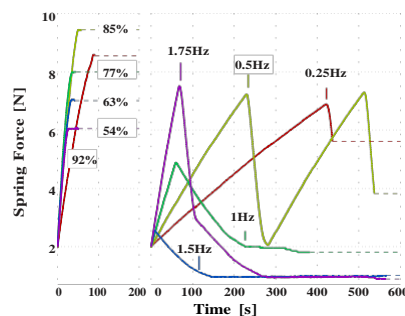
Methods: A prototype needle-driving robot, shown in Fig. 1(a), consisting of a rotor driving a gear train attached to a set of calibrated NiTi springs, was built and used for experiments. Custom real-time sequence and image reconstruction software that (1) interleaves imaging and actuation and (2) estimates the rotor angle position between imaging cycles was developed for a Skyra 3T Siemens scanner using the IDEA package. Maximum torque with closed-loop control was compared to open-loop control. The closed-loop tests varied the duty cycle time between actuation and imaging, and open-loop tests varied the driving sinusoidal frequency.

Results: Closed-loop control attains higher maximum forces and is up to twice as fast as the best open-loop control. Fig. 1(b) depicts maximum force for closed-loop experiments. The maximum output torque of $\sim 9\text{N}$ occurs for 84.6% of duty cycle. Fig. 1(b) depicts maximum force for open-loop experiments. A maximum output force of $\sim 7\text{N}$ was consistent for frequencies below 1Hz, however higher open-loop frequencies increased the probability of the rotor stalling without producing any force.

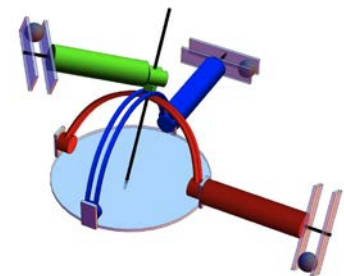
Conclusion: Generation of 9N of force using the actuation capability of an MRI scanner could enable new MRI guided interventions. Preliminary results suggest that multiple rotors can be simultaneously actuated and imaged. Future work will include the design of a portable and wireless biopsy robot that can orient, insert and image a needle completely under the control of an MRI scanner (design principle shown in Fig. 1(c)).



(a) prototype



(b) Closed- and Open-loop forces



(c) Biopsy robot design

Figure 1: Preliminary experiments with a prototype actuator capable of generating over 9N force in a Skyra 3T MR scanner. (b) Closed- (left) and open-loop (right) force experiment show the importance of accurate state estimation. (c) Control of multiple rotors for a three DOF biopsy robot design.

Real-Time Dynamic Scan Plane Control for Effective MRI-Guided Robotic Interventions

Mahamadou Diakite¹, Steve Roys¹, Taehoon Shin¹, Marc J Simard², Jaydev P Desai³, Rao P. Gullapalli¹

¹Center for Metabolic Imaging & Therapeutics, Department of Diagnostic Radiology and Nuclear Medicine, ²Department of Neurosurgery, University of Maryland School of Medicine, Baltimore, Maryland, United States, ³Department of Mechanical Engineering, University of Maryland, College Park, Maryland, United States

Purpose:

Real-time tracking and navigation is important for effective use of a robotic device with multiple degrees of freedom, and especially one that has multiple end effector functions including cauterization. The goal of this study is to develop a real-time MRI system for tracking the interventional device using a passive magnetic sensor and updating the slice location and orientation in real time. Its technical feasibility is demonstrated on a phantom.

Methods:

The MR imaging sequence consisted of radial readouts for rapid data acquisition and a set of bipolar tracking gradient waveforms which trigger a commercially available, miniature 3D magnetic field sensor (Robin Medical, Inc. Baltimore, USA) (Fig. 1). The overhead time for the tracking gradient was minimized by calibrating the gradient amplitude and slew rate. As a result, a temporal resolution of ~4 frames per second was achieved. A feedback loop mechanism was integrated into the MRI sequence that allowed the calculated

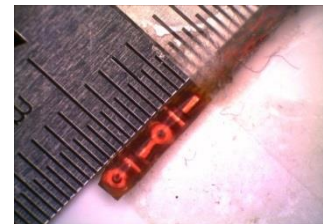


Figure 1: Position tracking sensor

Results:

Real-time navigation of the sensor under MRI-guidance was performed in a homemade phantom which consisted of a shaped piece of tubing immersed in water. Simultaneous imaging of the phantom with real-time update of a slice orthogonal to the direction of the sensor's movement was performed. Fig. 3 shows the trajectories of dynamic position of the sensor overlaid on a coronal image of the phantom. The dynamic position data are well correlated with the path through the phantom obtained from the MR images.

Conclusions:

We demonstrated the feasibility of real-time monitoring and tracking of a surgical robot under MRI guidance which allows a temporal resolution of 1x1x3 mm and a feedback latency of less than 10 ms. Quantitative validation of the tracking accuracy is under investigation using a motion platform which generates motion with programmed speed and acceleration.

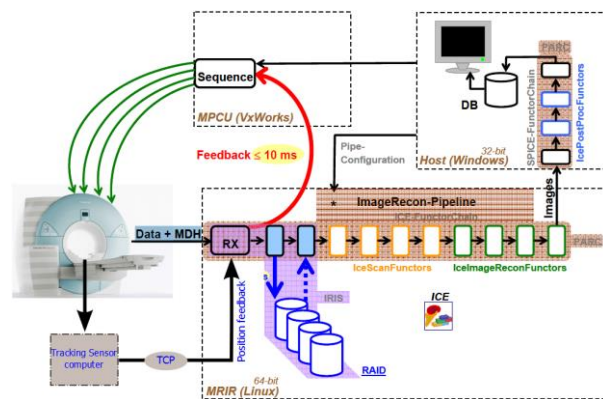


Figure 2: Schematic of the software architecture for real-time tracking and navigation

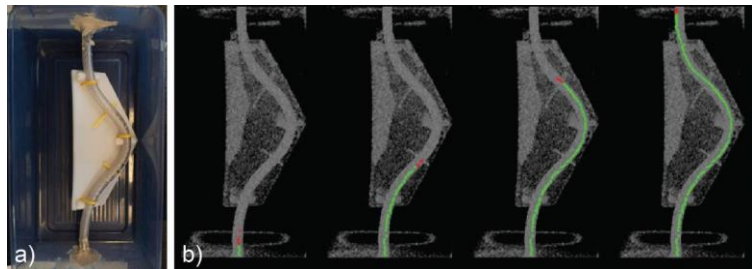


Figure 3: a) Picture of the test phantom. b) Real-time tracking of the sensor's positions at different time points.

Funding sources: This work was partially supported by NIH grants R01EB015870 and R01EB008713.

Fusion of laparoscopic ultrasound with MRI during robotically assisted nephrectomies

Samuel Kadoury¹, Jochen Kruecker², Pinter A Pinto³, and Bradford J Wood³

1 - Polytechnique Montreal, Montreal, Canada 2 – Philips Research North America, Briarcliff Manor, NY

3 - National Institutes of Health, Bethesda, MD

Background

During robotically-assisted nephrectomy procedures, the surgeon uses different imaging modalities such as a laparoscopic camera to view the organ, laparoscopic ultrasound (US) to visualize the tumor and MRI to verify the surgical plan of the resection. Image fusion would be beneficial to confirm the location of necrotic tissue prior to incision. We evaluated the feasibility of an automated image-based (MRI/US) registration technique during robot-assisted nephrectomy in patients with renal masses and examined fusion results in initial experiences.

Material and Methods

Prior to the image-guided intervention, the MR image volume of the diseased kidney is automatically segmented to obtain a 3D shape model of the kidney of interest. A shape-constrained deformable surface model is employed to guide the segmentation from the contrast-enhanced MR scan. Once the patient is in the operating room with the da Vinci (Intuitive surgical) in place, an input 3D US volume is created from an electromagnetically (EM) tracked kidney sweep. The kidney surface boundary at one of the lobe extremities is extracted using a confidence-based region-growing algorithm, which iteratively creates a binary volume by dynamically adapting the intensity range. Finally, registration is performed with a weighted ICP algorithm of the multimodal 3D surface models. Regional salient statistics are used as a data-related similarity term, seeking to align sub-regions to corresponding mesh surface.

Results

Two patients diagnosed with kidney cancer were included in this pilot study. 3D renal images were acquired on a Philips 3T Achieva MR scanner (Philips Medical Systems, Best, The Netherlands), with an endorectal coil. A CX-50 scanner (Philips Healthcare, Andover, MA) was used for US acquisitions. The laparoscopic L10-4 US transducer was tracked by using a 6-*dof* EM position sensor (Aurora, Northern Digital Inc., Waterloo, Ontario, Canada), which was attached to the handle of the transducer. The EM field generator was mounted on an articulated mechanical arm and placed over the patient during the procedure. For the overall registration workflow accuracy assessment, we established ground truth anatomical landmarks (2-4 per patient) evaluating landmark registration error (LRE) by carefully defining anatomical landmark fiducial point correspondences present on both US and MRI images. The average root-mean-square LRE (using these anatomical landmarks) was $3.2 \pm 0.8\text{mm}$ for the automatic registration. Sample registration results are provided in Figure 1.

Conclusion

Image based registration for robot assisted partial nephrectomy for renal masses was feasible in our early experience. Future work will investigate the performance on a larger cohort.

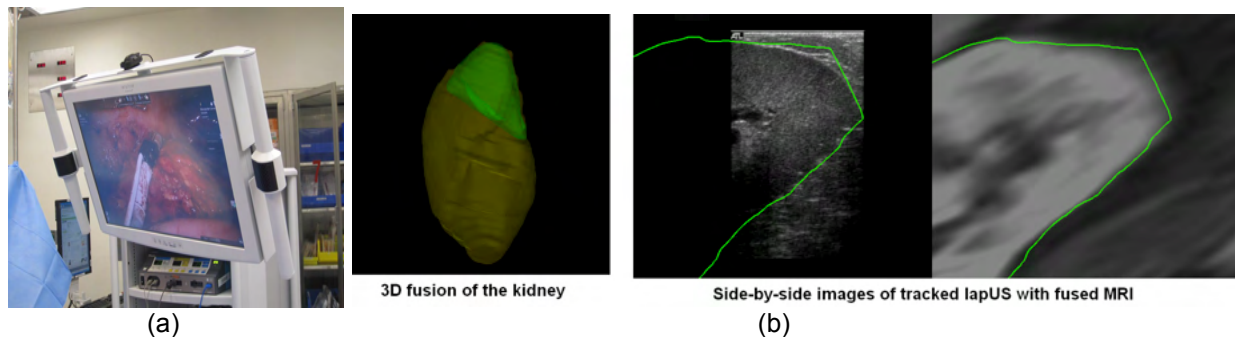


Figure 1. (a) Acquisition of ultrasound images with a laparoscopic probe. (b) Registration results with aligned segmented 3D models and side-by-side images of MRI and lapUS.

Lightfield 3D Endoscope for Minimally Invasive Surgery

Jason Geng
Xigen LLC

Purpose

Despite rapid advances in minimally invasive surgery (MIS) techniques, with significant number of successful procedures reported in literatures, visualization capability of existing laparoscopes/endoscopes proves problematic and inadequate, failing to provide true 3D perception and quantitative measurement capability for MIS surgeons. Studies showed that compared with surgeries under the direct normal vision, 2D endoscopic vision impaired surgical performance by 35% to 100%.

Current designs of stereo endoscopes offer very limited baseline to provide sufficient parallax for comfortable 3D viewing and for reliable 3D surface reconstruction. Acquiring only stereo images precludes the possibility of glasses-free 3D viewing experience where surgeons can move around without restricted viewing zone or console.

Methods

We have designed, built and tested a new concept of 3D endoscope, dubbed Lightfield 3D Endoscope, based on the lightfield principle. Instead of capturing only a stereo pair images, we designed a miniature endoscope that is able to acquire 8-ch high resolution images of a surgical scene simultaneously. This set of lightfield images not only can be used to facilitate realtime, large screen, high resolution and glasses-free 3D display during MIS surgery, they also enable full frame 3D reconstruction of surgical scene, thus providing surgeons with quantitative measurement and sizing capability. The precise surface reconstruction data also facilitate the image-guided therapy and augmented reality visualization via the precise registration of in vivo 3D surface data and pre-operative CT/MRI.

Results

A functioning prototype of the Lightfield 3D Endoscope was designed, built, and tested, with a miniature size of 10 mm in diameter and 80 mm in length(Fig 1). It is capable of capturing 8-channel video image with NTSC resolution, at 30HZ frame rate(Fig 2). 3D reconstruction algorithms and software were developed and implemented on GPU platform to process the lightfield images and reconstruct 3D surface profile at close to realtime frame rate(Fig 3).

Conclusions

A new concept of acquiring 3D surface image for MIS is proposed based on lightfield principle. A functioning prototype of the Lightfield 3D Endoscope was designed, built and tested for realtime 3D image capturing, reconstruction, visualization, and measurement. Experimental results demonstrated the new capabilities of capturing realtime lightfield images, reconstructing 3D surface, and registering with pre-operative data for MIS applications.

Funding Sources

Research reported in this publication was supported in part by NIBIB and NCI of NIH under award numbers R43 EB014598, R43EB016979, and N43-CO-2012-00031.

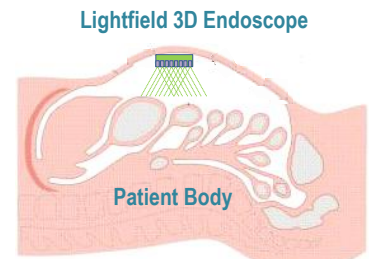


Fig 1. Illustration of the Lightfield 3D Endoscope for MIS

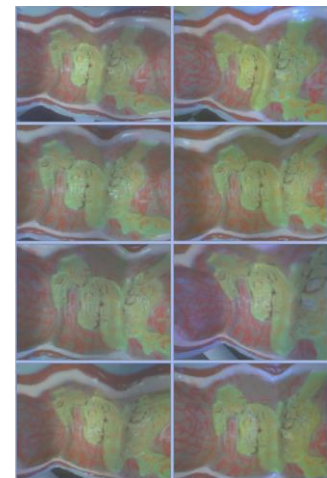


Fig 2. Images of a section of GI phantom captured by the 8-ch Lightfield 3D Endoscope

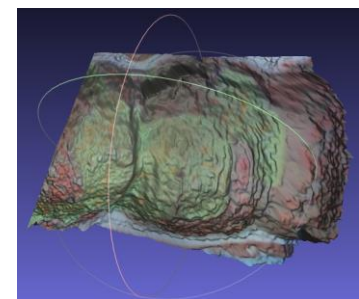


Fig 3. Reconstructed 3D surface of the GI phantom based on the lightfield Images captured by the 8-ch Lightfield 3D Endoscope

Implementing Therapeutic Dose-Volume Liver Response in Biomechanical Modeling

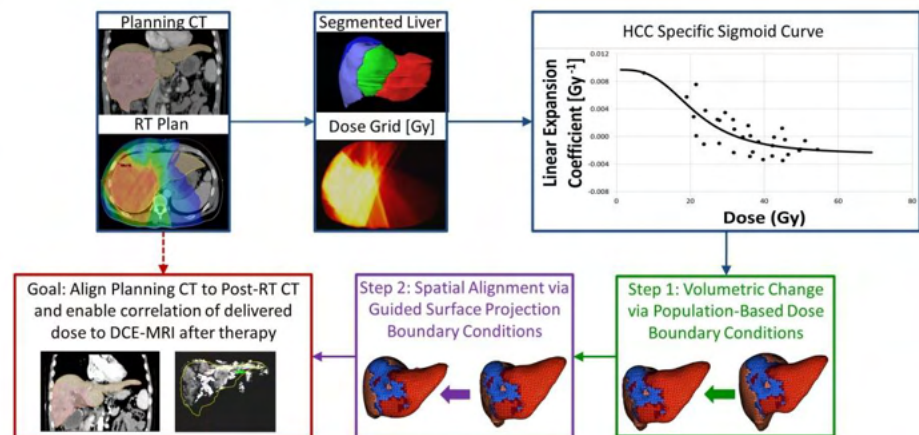
Authors: D. Polan¹, M. Feng¹, T. Lawrence¹, R. Ten Haken¹, K. Brock¹

Affiliation: ¹University of Michigan

Purpose: Understanding anatomical and functional changes of the liver resulting from therapeutic radiation treatment is fundamental to the improvement of normal tissue complication models needed for the advancement of personalized, evidence-based medicine. The ability to link pre-treatment and post-treatment imaging is often obscured by significant dose-based volumetric changes within the liver that are currently not accounted for in deformable image techniques. This study investigates using delivered dose, in combination with patient factors including tumor location, tumor type, and liver function, to biomechanically model liver anatomy changes over the course of radiation treatment and follow-up care.

Methods: Best-fit sigmoid functions, describing the relationship between dose and volumetric response, stratified by tumor location and type (biliary cancer (B), colorectal metastases (CR), and hepatocellular carcinoma (HCC)), were produced using retrospective data from 31 patients (10 B, 12 CR, and 9 HCC) treated with focal radiation therapy. The liver, tumor, and individual segments were contoured and thermal expansion coefficients were calculated for each segment based on individual volumetric change and mean dose. Finite element modeling and analysis was performed by modifying thermal expansion coefficients to represent the dose response,

and guided surface projections to represent spatial alignment. Evaluation of the model was done by comparing the model-predicted volumetric change within the liver to the observed change and by tracking identified pre-treatment vessel bifurcation



points within the liver through the deformation process, then determining target registration error (TRE) between the predicted final locations and identified post-treatment bifurcation points.

Results: Evaluation of the HCC-specific model (sigmoid curve $R^2 = 0.64$, Spearman Correlation $\rho = -0.67$ and $p < 0.0001$) was performed on a HCC patient with clinically significant volumetric changes within the liver following radiation treatment (total liver volume = -29%, tumor volume = -54%, normal liver = +7%). Deformable image registration in commercial treatment planning software predicted a total liver volume decrease of 17% (tumor volume = -16%, normal liver volume = -19%) with a TRE of 31.1 mm. Deformable image registration utilizing the dose-driven response model, showed vast improvement, predicting a total liver decrease of 26% (tumor volume = -49%, normal liver volume = +2%) with a TRE of 6.5 mm.

Conclusions: This work highlights the feasibility of implementing dose-driven volumetric response in deformable registration, enabling improved accuracy of modeling liver anatomy changes and correlating images over the course of therapeutic radiation treatment.

Funding: This research was funded in part by NIH PO1 CA59827 and R01CA124714-01.

Oxygenation Assessment in Residual Gynecologic Cancers after External Beam Radiation: Preliminary Characterization using T2* Mapping

Pelin A. Ciris, PhD¹, Antonio L. Damato, PhD², Clare M. Tempany-Afdhal, MD¹, Ehud J. Schmidt, PhD¹, Akila N. Viswanathan, MD, MPH² ¹Radiology and ²Radiation Oncology, Brigham and Women's Hospital, Boston MA, USA.

Purpose: To evaluate role of T2* mapping to identify hypoxic regions within gynecologic cancer remaining after external beam radiation therapy (EBRT).

Methods: Endogenous paramagnetic deoxyhemoglobin accelerates spin-spin relaxation in blood vessels and surrounding tissue. Assuming high deoxyhemoglobin reflects low oxygenation (O₂), a short apparent T2 (T2*) implies tissue hypoxia. Eleven patients with gynecologic cancers presenting for High Dose Rate brachytherapy following EBR therapy were imaged at 3T (Siemens, Verio). The protocol included T2-weighted turbo-spin-echo (TSE), pre and post-contrast enhanced T1-weighted and diffusion-weighted imaging (DWI). Multi-echo gradient-echo images were acquired for T2* mapping (TE= 3, 9, 18, 27, 36, 45ms) over multiple O₂ conditions while patients were breathing air mixed with O₂ through an endotracheal tube (30% to 100% O₂ in expired air). T2* maps were calculated by fitting an exponential function to signal intensity versus TE. Tumor and muscle regions were contoured on T2-TSE images, aided by post-contrast T1 and DWI (Figure). Contours were overlaid on registered T2* maps and shifted to account for motion. Outliers beyond ± 3 standard deviations (SD) of the median were excluded to eliminate registration errors, such as due to bladder filling. T2* values averaged over O₂ conditions are reported as mean \pm SD for each patient (Table). Hypoxic tumor burden is estimated as the percentage of tumor with T2* values shorter than the same patient's mean muscle T2*.

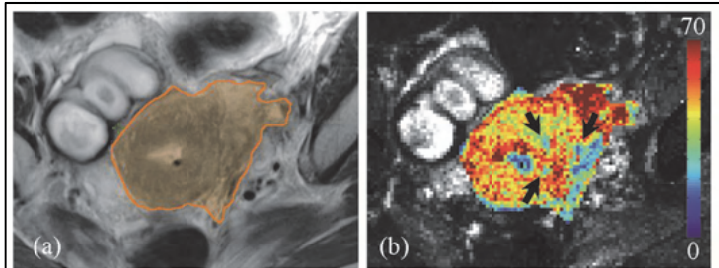


Figure: (a) Residual tumor contour on T2-TSE (b) T2* map & color overlay within tumor contour (ms). Arrows point to low T2* regions (T2* < 25ms) which may indicate hypoxic areas within tumor.

Results: Tumor and muscle T2* were very reproducible across O₂ conditions (mean of SDs: 1.1ms and 0.1ms, respectively). Muscle T2* was also consistent both across patients (20.3 \pm 2.7ms) and within each contour (SDs: 3-5ms). There was a large variation in tumor volumes (31.9 \pm 30.1 cm³) across patients. Unlike muscle T2*, tumor T2* varied both across patients (26.6 \pm 8.2ms) and within each contour (SDs: 8-16ms). Consequently, tumor fractions with T2* values shorter than the mean muscle T2*, potentially an indicator of hypoxic tumor burden, were very consistent across conditions for each patient (small SDs), but varied considerably across patients (48 \pm 21%).

Conclusion: T2* mapping is feasible in post EBRT residual gynecologic cancer. Marked variation across tumors as well as within tumors, relative to consistent muscle values, is encouraging for identifying hypoxic tumor regions, using muscle values as a threshold.

Table: T2* (ms) in tumor, muscle, and tumor fraction with T2* < muscle T2* (patient mean and SDs are across O₂ conditions). Mean and SD (across patients), and mean of the SDs (across O₂ conditions).

Patient	Tumor T2*	Muscle T2*	Hypoxic %
1	26.4 \pm 0.3	18.7 \pm 0.1	34 \pm 1
2	26.2 \pm 1.1	20.5 \pm 0.0	44 \pm 1
3	35.1 \pm 4.8	19.8 \pm 0.1	22 \pm 5
4	28.0 \pm 1.0	21.5 \pm 0.0	47 \pm 2
5	30.9 \pm 0.0	15.2 \pm 0.1	30 \pm 0
6	21.3 \pm 1.3	18.2 \pm 0.0	68 \pm 1
7	22.6 \pm 0.4	20.2 \pm 0.0	53 \pm 3
8	45.3 \pm 0.8	25.1 \pm 0.2	13 \pm 2
9	19.0 \pm 0.7	20.6 \pm 0.1	72 \pm 4
10	18.3 \pm 0.2	19.2 \pm 0.1	71 \pm 1
11	19.2 \pm 1.4	23.8 \pm 0.1	72 \pm 6
Mean	26.6	20.3	48
SD	8.2	2.7	21
Mean of SDs	1.1	0.1	2

Confocal Microscopy-guided Laser Ablation of Basal Cell Carcinomas

Heidy Sierra, Jason Chen, Anthony Rossi, Kishwer Nehal and Milind Rajadhyaksha
Dermatology Service, Memorial Sloan Kettering Cancer Center, New York, NY, USA

PURPOSE: Laser ablation is a promising approach for minimally invasive removal of superficial and early nodular basal cell carcinomas (BCCs). However, during the process, all target tissue is vaporized, leaving no tissue for immediate histopathological confirmation. We are conducting studies in human skin *ex vivo* and *in vivo* to investigate feasibility of a high-resolution nuclear-level optical imaging such as confocal microscopy (RCM) to guide laser ablation, with detection of residual tumor (histopathology-like confirmation) in post-ablated thermally coagulated tissue directly on patients.

METHODS: RCM imaging and ablation with a laser wavelength of 2.94 μm , pulse duration of 250 μsec , fluence of 25 J/cm^2 is being investigated. Fluence and number of pulses is being optimized, so as to control post-ablated thermal coagulation, to subsequently enable uptake of contrast agent and imaging to detect presence or clearance of residual BCCs after ablation. Sixty-eight human skin specimens immersed in acetic acid (5%, 30 seconds) for contrast, were imaged, ablated, once again immersed in acetic acid, imaged and finally processed for histopathology (Fig. 1). For the *in vivo* study, four lesions were imaged, ablated and imaged using 35% AlCl_3 for nuclear contrast (Fig. 2).

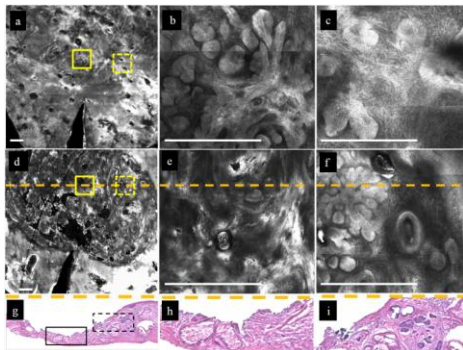


Fig.1. RCM imaging detects clearance and presence of residual BCC tumor in skin specimens, after ablation with 6 passes. (a)-(c) Pre-ablation images showing presence of tumor. (d) Post-ablation RCM mosaic. (e) Clearance and (f) presence of tumor from solid and dashed squares respectively. (g)-(i) Vertical histopathology confirms findings in RCM images (from location of the yellow lines). Bars= 500 μm .

RESULTS: For the *ex vivo* study, qualitative evaluation of RCM images against the corresponding histopathology for the appearance of ablated skin showed that a total delivered fluence of up to 150 J/cm^2 allows repeatable and consistent results. Quantification of the accuracy of RCM to detect the clearance or presence of tumor after ablation in fifteen specimens shows 77% agreement with histopathology and a negative predictive value of 0.8 for 10 specimens. *In vivo* testing shows similar results to those obtained in the *ex vivo* study.

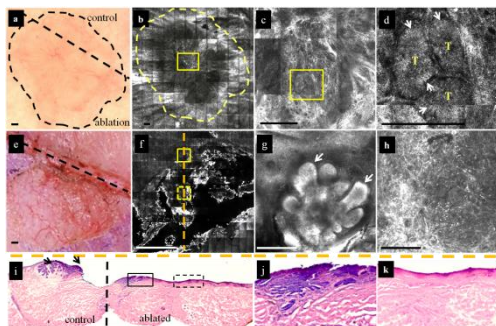


Fig. 2. RCM imaging detects clearance and presence of residual BCC tumor in skin *in vivo*, with 6 passes. (a) A dermoscopy image, showing the selected areas for ablation and control. (b) Pre-ablation RCM image of the lesion. (b)-(d) Enlarged views of the yellow square in (c) show BCCs tumor islands (T). (e) A post-ablation clinical image. (f) Post-ablation RCM image of the lesion. (g) residual tumor and (h) normal dermis in solid and dashed squares in (f). (i)-(k) Vertical histopathology confirms findings in RCM images (at the location of yellow lines). Bars= 250 μm .

CONCLUSIONS: These results suggest that imaging may guide laser ablation and enable less invasive treatment via localized control on the depth of ablation. Further investigation and optimization of this approach to enhance tumor-to-dermis contrast is necessary.

***In vivo* Confirmation of THz Wound Edema Imaging for Burn Surgery Using MR**

Neha Bajwa^{1,3}, Shijun Sung^{2,3}, James Garritano³, Priyamvada Tewari^{1,3}, Bryan Nowroozi^{1,3}, Zachary Taylor^{2,3}, Alexander Stojadinovic⁵, Jeffrey Alger⁴, and Warren Grundfest^{1,3}

¹Department of Bioengineering, University of California, Los Angeles, CA, ²Department of Electrical Engineering, UCLA, CA, ³Center for Advanced Surgical and Interventional Technology (CASIT), Dept. of Surgery, UCLA ⁴Department of Neurology, UCLA, CA, ⁵ Walter Reed Army Medical Center, Department of Surgery, Washington, DC

Purpose: Terahertz (THz) detection has been proposed for a variety of medical imaging applications in view of its hydration profiling capabilities. Recent *in vivo* studies suggest that THz sensing can be used to identify burn wound severity in rats as early as 30 minutes following thermal injury. The power of THz imaging of burns lies in its ability to transform what is inferred to be edema, an imaging confounder to all other diagnostics, into a contrast mechanism enabling the technology to provide accuracy in the acute phase of the wound response. For this technology to gain traction as a comprehensive burn guidance tool, further investigation of the contributions from tissue pathology to THz imaging contrast using a parallel imaging modality is required. MRI offers a means to visualize water ingress and egress in skin layers, and can therefore be utilized to verify the spatiotemporal evolution of burn wound edema in THz imaging.

Methods: Parallel T2 weighted multi slice multi echo (T2w MSME) 7T MR scans and THz surface reflectance maps were acquired of a full thickness skin burn in an *in vivo* rat model. Extrinsic tattoo ink fiducial markers were intradermally injected in the abdomen, a 2 mm x 19 mm rectangular brand was heated to 200°C, a full thickness burn was induced on the abdomen of an anesthetized rat, and scans covering a 2.5 x 2.5 cm and 4 cm x 1 cm field of view were initiated with the THz and MR imaging systems, respectively, every hour for the next 5 hours. A 12 µm thick Mylar window was lowered onto the burn during THz imaging to isolate hydration contrast from all other skin features.

Results: Acquired *in vivo* THz imagery of a skin burn, shown in Figure 1, delineates significant changes in THz reflectivity within burn zones during the first few hours following burn induction. THz image sets are displayed in a standard false color map where red denotes increased reflectivity while blue indicates a decrease. THz and MRI imagery of the rat abdomen prior to burn induction displays a somewhat uniform reflectivity and average T2 relaxation times of the epidermis, dermis, and hypodermis layers that are characteristic of uninjured skin, respectively. Immediately following thermal insult, the THz burn image shows a clearly defined, central burn region of low reflectivity. Parallel T2w MSME imagery of the wound demonstrates localization of the burn site as well as small changes in T2 relaxation times within the burn. Comparison of imagery prior to burn induction and at the 3.5 hour mark suggests a growing increase in both reflectivity and T2 relaxation times in response to an influx of edematous fluid to the burn site. Redistribution of perfusion in the central region of the burn continues to grow by the 4.5 hour mark of the burn response, with a 15 % and 3-fold increase in reflectivity and T2 relaxation times, respectively.

Conclusions: Burn tissue regions identified by their hydration content using MR imaging spatially map to those in THz burn images, offering a way to verify the edematous response. These efforts support the clinical translation of THz burn wound edema imaging as a diagnostic burn imaging tool.

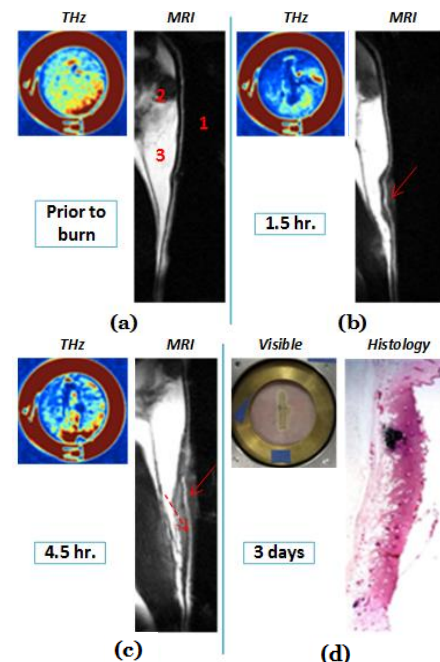


Figure 1: THz reflectivity and sagittal MR imagery (a) prior to burn, (b) 1.5 hr, and (c) 4.5 hr following burn induction. In (a) the labels are: (1) Epidermis, (2) Dermis, and (3) Hypodermis. Localization of the burn and fluid ingress are demarcated by solid and dashed arrows, respectively in (a) - (c). (d) Visible and H & E imagery of a 200°C burn in rat.

Magnetically Assisted Remote-controlled Endovascular Catheter for Interventional MR Imaging: In Vitro Navigation at 1.5 T versus X-ray Fluoroscopy

Aaron D. Losey, Prasheel Lillaney, Alastair J. Martin, Daniel L. Cooke, Mark W. Wilson, Bradford Thorne, Ryan S. Sincic, Ronald L. Arenson, Maythem Saeed, Steven W. Hetts, MD — Radiology, UCSF

Purpose: To compare in vitro navigation of a magnetically assisted remote-controlled (MARC) catheter under real-time magnetic resonance (MR) imaging with manual navigation under MR imaging and standard x-ray guidance in endovascular catheterization procedures in an abdominal aortic phantom.

Materials and Methods: The 2-mm-diameter custom clinical-grade microcatheter prototype with a solenoid coil at the distal tip was deflected with a foot pedal actuator used to deliver 300 mA of positive or negative current. Investigators navigated the catheter into branch vessels in a custom cryogel abdominal aortic phantom. This was repeated under MR imaging guidance without magnetic assistance and under conventional x-ray fluoroscopy. MR experiments were performed at 1.5 T by using a balanced steady-state free precession sequence. The mean procedure times and percentage success data were determined and analyzed with a linear mixed-effects regression analysis.

Results: The catheter was clearly visible under real-time MR imaging. One hundred ninety-two (80%) of 240 turns were successfully completed with magnetically assisted guidance versus 144 (60%) of 240 turns with nonassisted guidance ($P < .001$) and 119 (74%) of 160 turns with standard x-ray guidance ($P = .028$). Overall mean procedure time was shorter with magnetically assisted than with nonassisted guidance under MR imaging (37 seconds \pm 6 [standard error of the mean] vs 55 seconds \pm 3, $P < .001$), and time was comparable between magnetically assisted and standard x-ray guidance (37 seconds \pm 6 vs 44 seconds \pm 3, $P = .045$). When stratified by angle of branch vessel, magnetic assistance was faster than nonassisted MR guidance at turns of 45°, 60°, and 75°.

Conclusion: In this study, a MARC catheter for endovascular navigation under real-time MR imaging guidance was developed and tested. For catheterization of branch vessels arising at large angles, magnetically assisted catheterization was faster than manual catheterization under MR imaging guidance and was comparable to standard x-ray guidance.

Reference: Losey AD, Lillaney P, Martin AJ, Cooke DL, Wilson MW, Thorne BR, Sincic RS, Arenson RL, Saeed M, Hetts SW. Magnetically Assisted Remote-controlled Endovascular Catheter for Interventional MR Imaging: In Vitro Navigation at 1.5 T versus X-ray Fluoroscopy. *Radiology*. 2014 Jun; 271(3):862-9.

Funding: NIBIB R01EB012031 (SWH), NIHMD R25MD006832, NCATS UL1 TR000004.

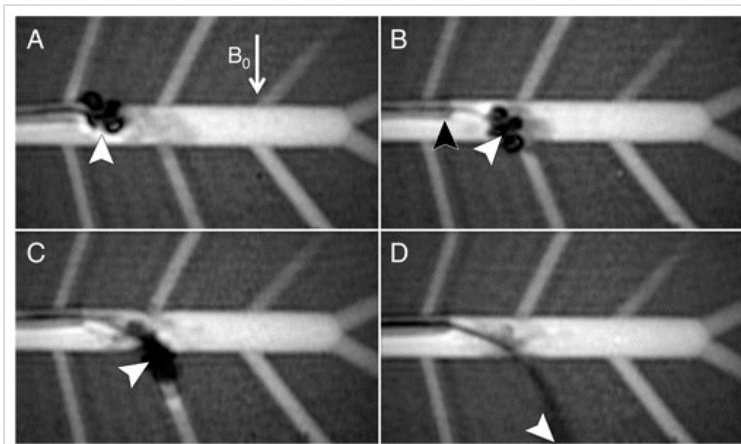


Figure 1: Coronal MR images of catheter deflecting into branch vessel arising at 60° from the parent vessel. *A*, Catheter tip (white arrowhead) became visible by delivery of current to microcoil and, *B*, deflected instantaneously while the guide catheter (black arrowhead) remained stationary. *C*, Then the interventionalist advanced the catheter forward to enter a vascular branch angled 60° to the parent vessel, *D*, turning off the current once the tip was within the branch vessel and manually advancing the catheter in the branch vessel to the edge of the vascular phantom.

How New High-Resolution Detector Systems can have High Impact on Minimally Invasive Image-Guided Interventions

S Rudin, DR Bednarek, CN Ionita, Swetadri Vasan S. N.

University at Buffalo, Toshiba Stroke and Vascular Research Center

Purpose: To highlight the great advances in high spatial-resolution x-ray detector technology and its dramatic impact on the course of endovascular interventional procedures such as minimally invasive treatment of aneurysms.

Methods: At critical stages during endovascular interventions, images with resolution higher than provided by commercially available state of the art detectors are proving to be greatly beneficial. Three new high resolution x-ray imagers were investigated with the following pixel sizes: Hamamatsu (Ham) 100 μm , Dexela (Dex) 75 μm , and the custom-designed and built Micro-angiographic Fluoroscope (MAF) 35 μm . The MAF was installed on a motorized changer in a clinical neuro-vascular suite as shown in Fig. 1 so as to be deployable below the standard



Fig. 1

flat panel detector (FPD) having 194 μm pixels. Image sequences from clinical interventions that were improved using a high-resolution detector will be shown. A new metric was created to enable quantitative comparison between the detectors for specific imaging

tasks. The Relative Object Detectability (ROD) is the ratio between detectors of the integral over spatial frequency (u,v) of the object Fourier Transform, $|\text{OBJ}(u,v)|^2$ and the detective quantum efficiency (DQE) of each detector. The metric can be generalized by including scatter and geometric unsharpness due to focal spot blur and magnification using generalized DQEs.

Results: Fig. 2 shows the great improvement for stent visualization over the FPD (a) when using the MAF (b). An image frame of a clinical aneurysm case in Fig. 3 shows detailed information of the texture of the coil being deployed into the aneurysm and the degree of filling of the aneurysm dome, all of which were unavailable in standard FPD imaging. This information was critical and saved this patient the need for a stent placement. The graph of ROD in Fig. 4 quantifies the improved detectability for spheres as a function of sphere diameter for three detectors compared to the standard FPD.

Conclusions: Higher resolution and more detailed imaging of the treatment devices have led to more accurate interventions in less time with less radiation dose, and will enable the use of new, more complicated interventional devices such as asymmetric stents.

Support: NIH NIBIB Grant R01EB002873

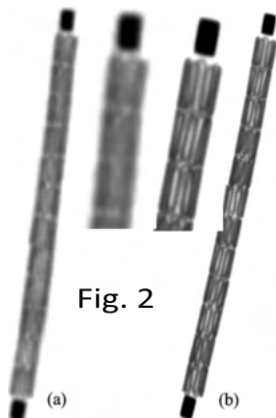


Fig. 2

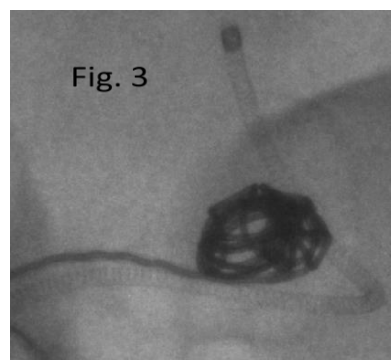
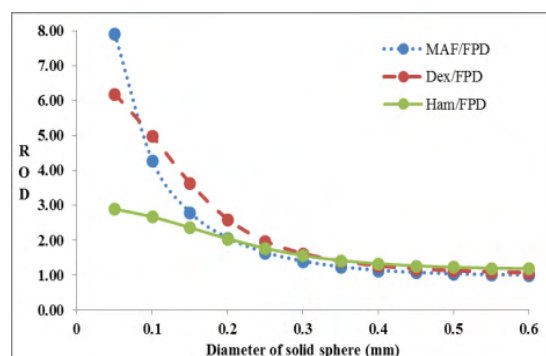


Fig. 3



Positive contrast spiral imaging of a nitinol guidewire

Adrienne E Campbell-Washburn, Toby Rogers, Robert J Lederman, Michael S Hansen and Anthony Z Faranesh

Cardiovascular and Pulmonary Branch, National Heart, Lung and Blood Institute, National Institutes of Health, Bethesda, MD, USA

PURPOSE: MRI-guided cardiovascular catheterization is appealing to reduce ionizing radiation exposure and improve tissue contrast. Clinical translation has been limited by the unavailability of MRI-visible and safe devices. In particular, rigid metallic guidewires are an essential device with a high risk of heating during MR imaging.¹ Here, we develop an MRI method to improve the MRI visualization of commercially available nitinol guidewires with negligible heating.

METHODS: Gradient echo spiral MR imaging was used to generate high frame rates with minimal heating (8 interleaves, TE/TR = 0.86/10ms, flip angle = 10°). Positive contrast was generated using through-slice dephasing² such that the nitinol guidewire appeared hyperintense while background signal was suppressed. An interleaved acquisition of a standard spiral image and a dephased spiral image generated an anatomical image and a device image in alternating frames. A 0.035" nitinol guidewire (Nitrex, Covidien, Plymouth, MN) was placed in the aorta of a swine to perform proof-of-concept *in vivo* testing. Animal experiments were approved by the institutional animal care and use committee according to NIH guidelines.

RESULTS: A pair of anatomical and device images can be generated with a temporal resolution of 160 ms (80 ms per image), or 6.25 frames/s. Figure 1 demonstrates the anatomical and device images generated from the spiral acquisitions. Signal thresholding of the device image was used to isolate the guidewire signal and overlay it onto the anatomical image (Figure 1c). This spiral imaging scheme generated a maximum temperature increase of 0.73°C during 1 minute of continuous imaging of a nitinol guidewire³ in a gel phantom.

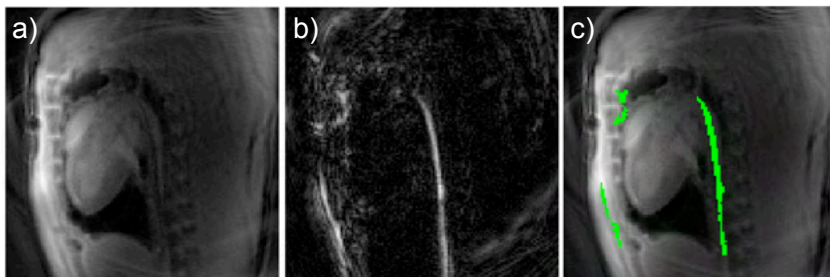


Figure 1: Anatomical image (a) and device image (b) generated with the interleaved spiral imaging scheme, and color overlay of the device on the anatomical image (c) for improved visualization.

CONCLUSIONS: Spiral imaging generated negligible heating of the nitinol guidewire. Through-slice dephasing before the spiral readout was able to produce *in vivo* positive contrast, as an improvement over traditional signal-void visualization. A color overlay of the device, with minimal artifact, can be generated using simple thresholding to assist in procedural guidance.

This method simultaneously improves device visualization and minimizes heating caused by rigid metallic guidewires, and therefore may permit the safe and effective use of commercially available guidewires for MRI-guided catheterizations.

REFERENCES: [1] Konings MK, et al, Heating around intravascular guidewires by resonating RF waves (2000). *J Magn Reson Imaging* 12 (1):79-85, [2] Seppenwoolde JH et al, Passive Tracking Exploiting Local Signal Conservation: The White Marker Phenomenon (2003). *MRM* 50:784-790. [3] Sonmez M et al. MRI active guidewire with an embedded temperature probe and providing a distinct tip signal to enhance clinical safety (2012). *J Cardiovasc Magn Reson*.

FUNDING: This work was supported by the NHLBI DIR (Z01-HL006039-01, Z01-HL005062-08)

MRI-based computer models using T1-mapping for guiding EP interventions

Mihaela Pop^{1,2}, Maxime Sermesant³, Samuel Oduneye^{1,2}, Sophie Giffard-Roisin³, Sebastian Ferguson¹, Labonny Biswas¹, Jen Barry¹, Eugene Crystal¹, Nicholas Ayache³, Graham Wright^{1,2}
¹Sunnybrook Research Institute (CA), ²Medical Biophysics, Univ. Toronto (CA), ³Inria - Aslepios project (FR)

Predictive image-based cardiac computer models can help us understand how the peri-infarct triggers lethal arrhythmias (such as ventricular tachycardia, VT) and how to optimize the guidance of electrophysiology (EP) interventions to eradicate malignant VT substrate; however, such *in silico* models require detailed validation and customization prior to their integration into the clinical platforms. Our previous efforts were focused on developing 3D MRI-based models using anatomy, infarct morphology and fiber directions obtained from diffusion-tensor (DT) images of explanted swine hearts, and on parameterizing these models from conventional electro-anatomical CARTO-EP recordings [1]. The next logical step is to build fast models using *in vivo* MR images; however, *in vivo* cardiac DTI is difficult to implement due to heart motion. Alternatively, here we propose a novel preclinical experimental-theoretical framework (Fig. 1) that integrates: 1) 3D heart anatomy, synthetic fibers, and infarct areas (i.e., scar and peri-infarct) determined from multi-contrast late enhancement (MCLE) images using steady-state and T1* maps, and 2) EP measurements obtained using a real-time MR-guided EP system (Imricor) visualized using *Vurtigo* (www.vurtigo.ca) [2]. For finite-element simulations of cardiac electrical activity, we generated 3D volumetric meshes (from stacks of segmented 2D images) using CGAL libraries, and then assigned a different electrical conductivity value per zone (i.e., normal myocardium, slow-conductive peri-infarct and non-conductive scar). Next, we simulated the propagation of depolarization wave through the cardiac tissue using a mono-domain macroscopic formalism [3]. Here, we used a 4,096 (1x) MB machine with an Intel® Core™ i3-2310M processor, 640 GB HD, NVIDIA® GeForce® 315M graphic adapter. For instance, the computational time required to simulate 0.3s of the cardiac cycle using fast eikonal equations was 10s for a mesh of 105K tetrahedral elements (~ 0.8mm element size) generated from a left ventricular slab (1cm-thick), and about 25s on a mesh of 300K elements (~1mm element size) for a full ventricle. Our results demonstrated the feasibility of constructing MCLE-based computer models, with computational times attractive to clinical interventions. Advantageously, the co-registration of MR and EP data using the real-time MR-EP system, can provide a more accurate model personalization compared to that obtained using CARTO data. Future work will focus on simulating the wave propagation in the presence of RF ablation lesions and on optimizing the planning of real-time MR-guided EP therapies, to eradicate the VT substrate.

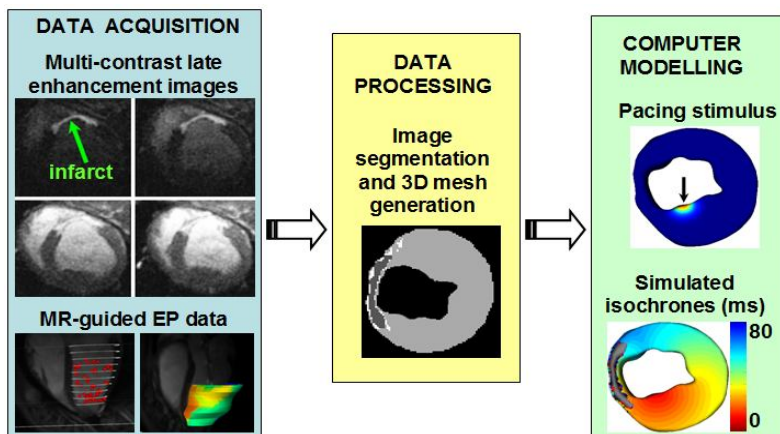


Figure1. Diagram of the experimental-theoretical framework to predict wave propagation and transmural depolarization times in the heart, using MCLE imaging-based models.

Reference: [1] Pop *et al*, LNCS (Springer) vol 7746, 2013, [2] Oduneye *et al*, IEEE-TBME 60(9), 2013, [3] Sermesant *et al*, IEEE-TMI 25(5), 2006.

Acknowledgement: Canadian Institutes of Health Research grant (MOP 93531).

Vascular Repair by MR RF Coagulation

Ouri Cohen,^{1,2,3} Erez Nevo,⁴ R. Gilberto González,^{1, 2,3} Albert J. Yoo,^{2,3} Jerome L. Ackerman^{1,2,3}
¹Martinos Center and ²Dept. of Radiology, Massachusetts General Hospital, Charlestown, MA;
³Harvard Medical School, Boston, MA; ⁴Robin Medical, Inc., Baltimore, MD

Purpose Current treatment methods for vascular defects such as aneurysms, include surgical clipping or endovascular embolization with coils, particles or a coagulable material such as Onyx (Micro Therapeutics Inc.). These methods entail either highly invasive surgery or the introduction of foreign bodies or materials into the patient. Previous research has successfully demonstrated ablation of tissue using RF energy harvested during MRI scanning. In this work we present a proof-of-concept for the embolization of aneurysms through MRI scanner-induced coagulation of an albumin protein solution, whose human equivalent is naturally present in blood thus eliminating the possibility of an immune reaction.

Methods To demonstrate the feasibility of coagulating albumin via the MR scanner, simulations of the heating and coagulation process were conducted, and experiments were performed on a Magnex 15T 130 mm horizontal bore magnet interfaced to a Siemens clinical MR console, and on a Siemens Avanto 1.5T clinical MRI scanner. Saline, simulating blood, was flowed through a glass aneurysm phantom. A 26 AWG Teflon insulated silver-plated copper wire with a 1.5 cm exposed tip, which could be the guidewire in an interventional procedure, was introduced into the aneurysm along with a catheter and a fiber-optic temperature sensor. When the MR scanning begins, the wire tip undergoes RF heating which is controlled by the RF duty cycle of the turbo spin echo pulse sequence. A solution of protein (egg white ovalbumin) was delivered into the simulated aneurysm.

Results Simulations using HFSS showed significant heating of the wire tip when driven by a tuned loop coil with the wire immersed in a medium with the electrical properties of blood (Figure 1). In experiments with the aneurysm phantom, a protein coagulum was readily produced when the temperature at the wire tip exceeded about 60 °C (Figures 2 and 3).

Conclusions Coagulation of a protein solution delivered by catheter into an aneurysm phantom can be achieved with RF heating in an MRI scanner. Experiments to follow will include live animals using an experimental model for aneurysm.

Funding Support was provided by Center for the Integration of Medicine and Innovative Technology (CIMIT) grant 13-1180/grant W81XWH-09-2-001 from U.S. Army Medical Research and Materiel Command (USAMRMC), Robin Medical, Inc., NIH grants RR023009 and P41RR14075, and the Athinoula A. Martinos Center for Biomedical Imaging.

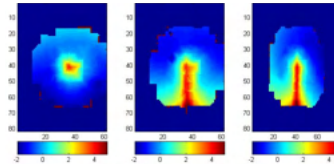


Figure 1. SAR maps of a wire tip embedded in a medium with the electrical properties of blood with the other end of the wire driven by a resonant loop coil in the MRI scanner.

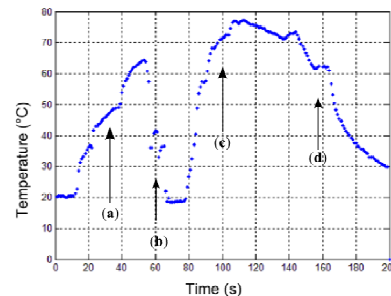


Figure 2. The four stages of the coagulation procedure are shown in this temperature profile. Saline preheating (a) was followed by albumin injection (b). After coagulation (c) the saline was allowed to return to room temperature (d). Note the rapid rise of temperature when the injection stops.

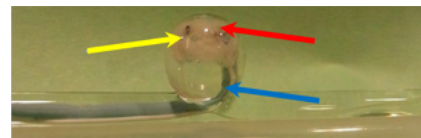


Figure 3. Protein coagulum (red arrow) generated in the glass aneurysm phantom by RF heating of a wire (blue arrow) during MRI scanning. The fiber optic temperature sensor is visible at the yellow arrow.

ABSTRACTS FOR POSTER PRESENTATIONS

Finite element based biomechanical analysis of cranial shapes for craniosynostosis surgical correction

Ricardo Ortiz², Andrew C. Bauer², Andinet Enquobahrie², Nabile M. Safdar¹, Gary F. Rogers¹, Marius George Linguraru¹

¹Children's National Medical Center, Washington DC, USA

²Kitware, Inc., Clifton Park, New York USA

Purpose: Currently, the decision of performing surgical correction for pediatric patients with craniosynostosis is typically based on subjective visual assessments. These decisions have a major impact on the management of these young patients requiring surgical intervention. In this paper we present our preliminary work on biomechanical finite element modeling based on the physical properties of the bone. The computed shape and stresses can then be used to evaluate and compare individual bone correction plans without carrying out the actual surgeries. Our overall objective is to design, develop, and validate a virtual surgery system for optimal treatment planning of craniosynostosis correction.

Methods: Two CT scans from a craniosynostotic pediatric patient were binarized to extract the skull and used to create the models: one of a malformed skull before surgery, and the other of the desired post-correction shape. A tetrahedral mesh was generated for each image using Cleaver, a tetrahedral mesh library. A displacement field was created between the exterior surfaces of both skull meshes. This displacement field was then used to apply a constant pressure field of about 20 MPa on the outer surface. The skull bones were assumed to be made of an elastic isotropic material with Young's modulus of 380 MPa and Poisson's ratio of 0.22. The base of the model, depicted by blue dots on Figure 1a (left), was kept fixed in order to support the mesh in place. The finite element method is implemented in the SOFA library. ParaView was used to visualize the results.

Results: With the proposed computational model the stress, strain and deformations produced by the change in geometry were computed. Figure 1 shows displacement maps and Von Mises stresses due to the deformations. The intensity of the displacement in Figure 1b can be seen more pronounced on those areas around the forehead topping at about 4mm where the biggest deformation is happening with a corresponding stress distributions of about 29 MPa, Figure 1c. The computed stresses for this craniosynostotic patient are significantly lower than the maximum allowable stress of 87 MPa.

Conclusions: We employed readily available open source software to model deformations on the skull and computed stresses occurring during these deformations. Physics based quantitative model can assist clinicians in determining what role the cranial shape should play in the decision to operate and could play a major factor in reducing the number of unwarranted surgical procedures, shortening the length of the intervention, and accurately comparing the outcomes of different surgeons and surgical techniques.

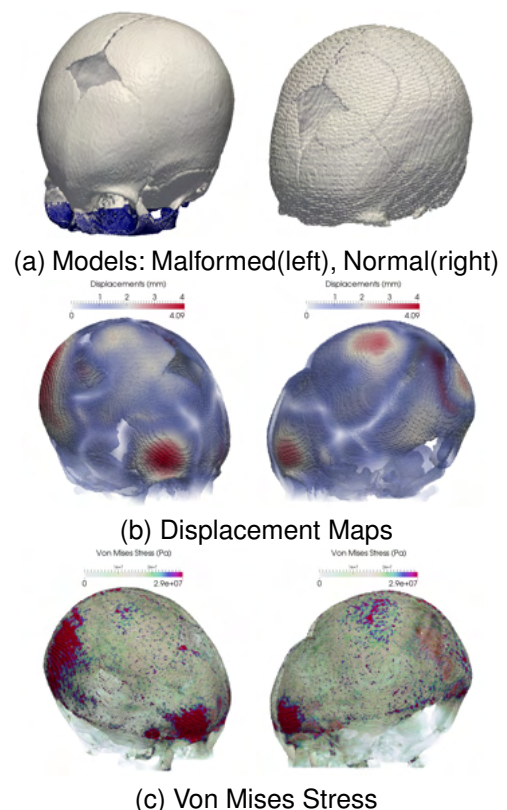


Figure 1: Models and computed displacement(mm) and stress distributions(Pa).

Tissue characterization and blurring identification in temporal lobe epilepsy

Luiz O. Murta Jr. and Ron Kikinis

Brigham and Women's Hospital

Purpose:

Temporal Lobe Epilepsy (TLE) with hippocampal sclerosis affects other mesial temporal lobe structures, showing the change in signal intensity of white matter (WM) and gray matter (GM) of Magnetic Resonance Imaging (MRI) in patients with TLE. Such abnormalities of signal intensity changes in the temporal lobes, or losses of marking between WM and GM are referred as blurring in literature (Kuba et al. 2012). TLE is the most common type of refractory epilepsy in adults, and thus strong candidate to surgery.

Methods:

This work investigates a method to detect presence of the epileptogenic tissue in temporal lobe by analyzing patterns of texture in MRI. Once segmented, the images are analyzed using texture descriptors from the intensity histogram and local pixels dependence measures proposed by Haralick (Haralick 1979). Subsequently, we investigated the set of feature vectors from the segmented GM using two classifiers in WEKA environment (Witten et al. 1999): artificial neural network and decision tree. We evaluated this method using a set of images from 32 patients with TLE, 15 of those exhibiting blurring and 17 without blurring in MRI observed at TL tissue. In whole process, a set of 98 planar images were considered for classification, and 51 are classified in "with blurring" category and 47 "without blurring" category. Both classifiers were evaluated regarding accuracy, and the one based on decision tree had the best and most valuable results. 32 different feature measurements have been used to construct descriptors vectors of segmented images. 24 features were extracted from the co-occurrence matrix using Haralick texture descriptors and 8 were MRI intensity statistics obtained from image histogram. When evaluating performance of the classifiers learning process, a basis of 70 planar images samples for training and 28 samples for test.

Results:

Results have shown decision tree having the highest precision and accuracy. Area under the ROC curve was found to be 71.42 %. As result of classifier optimization, from preselected 32 texture feature descriptors, 6 descriptors were shown to be relevant for classification of TL tissues.

Conclusions:

From the found results, one can concludes that lateral asymmetry on grey level co-occurrence homogeneity and entropy measures, as well as histogram statistical descriptors, i.e. mean grey level, standard deviation, and kurtosis are relevant to blurring identification decision. These texture descriptors were observed on temporal lobe GM, and can provide automatic identification or indicate what image features neurologists should be aware of while observing suspicious MRIs.

References:

- Haralick, R.M., 1979. Statistical and structural approaches to texture. *Proceedings of the IEEE*.
- Kuba, R. et al., 2012. Grey-white matter abnormalities in temporal lobe epilepsy associated with hippocampal sclerosis: Inter-observer analysis, histopathological findings, and correlation with clinical variables. *Epilepsy Res*, 102(1-2), 78-85.
- Witten, I.H. et al., 1999. Weka: Practical machine learning tools and techniques with Java implementations.

Title: Mutual Information Registration of MRI for Neurosurgical Applications

Authors: Meysam Torabi, Anil Shetty, and Ashok Gowda

Affiliation and Funding: Visualase, Inc., 8058 El Rio St., Houston, TX 77054

Background and Purpose: Visualase offers a minimally-invasive MRI-guided surgical system by utilizing laser-induced interstitial thermal therapy (LITT), which has gained importance recently. The company is developing a software platform technology to enable the user to co-register various image data sets of the patient during the planning, monitoring and confirmation stages. In this work, we quantitatively validate the feasibility of using mutual information registration for brain tumor and epilepsy treatment applications.

Methods: A mutual information registration [1] was used to register T1 and T2 MR images. 7 patients were randomly selected and enrolled in the experiment creating 21 image datasets, which were acquired either on the same day or within a time interval. The registration parameters were tuned so as to maximize images alignment. The optimal parameters, number of samples and histogram bins, were set to 50000 and 50 respectively. To facilitate the usage of the registration in clinics, no manual masking was used and hence the entire brain was registered. Since, in the planning, monitoring and confirmation stages, different MRI's may be acquired, 5 types of registration were performed: a) T1 image to T1 image, b) T1 image to T2 image, c) Volumetric image data to limited image data, d) Volumetric image data to volumetric image data, and e) Image data of the same patient from different time points (from 2 days to 7 months). The user initialized the registration using a linear transformation to compensate for major motions of the patient, and then rigid, ScaleSkewVersor3D and affine registrations were sequentially applied to produce the final moving image. 3D Slicer, an open source software, was used to visualize the results [3].

Results: After the initialization, the registration process for each dataset took ~10 seconds. A quantitative accuracy analysis was conducted using Targeting Registration Error (TRE) [2] with 3 fiducial markers distributed over the brain; the overall TRE of 63 pairs of the fiducials was 2.5 mm. As well, TRE was calculated for the 5 above-mentioned categories, and were calculated to be: a) 2.2 mm, b) 2.42 mm, c) 2.54 mm, d) 2.15 mm, and e) 2.55 mm, respectively.

Conclusions: The acceptable accuracy, the speed of the registration, and the capability of the registration to handle different types of datasets (such as registration of volumetric MRI to limited slices) make this registration useful in clinics. The results demonstrated the potential of using the mutual information registration for brain tumor and epilepsy treatment applications. We consider studying GPU-based registrations, such as the one in [4], to accelerate the registration further to be able to actively register incoming monitoring images in a real-time manner during therapy which essentially eliminates any patient movements.

[1] Johnson H.J., Harris G., Williams K, "BRAINSFit: Mutual information registrations of whole-brain 3D images, using the insight toolkit", 2007, the insight journal.

[2] Fitzpatrick J.M., West J.B.. "The distribution of target registration error in rigid-body point-based registration.", IEEE Trans Med Imaging. 2001 Sep;20(9):917-27.

[3] S. Pieper, B. Lorensen, W. Schroeder, and R. Kikinis, "The NA-MIC kit: ITK, VTK, pipelines, grids and 3D Slicer as an open platform for the medical image computing community," in Proc. IEEE 3rd Int. Symp. Biomed. Imag.: From Nano Macro, 2006, pp. 698-701.

[4] Liu Y., Fedorov A., Kikinis R., Chisochoides N., "Real-time non-rigid registration of medical images on a cooperative parallel architecture, pp401-404., IEEE International Conference on BIBM, 2009.

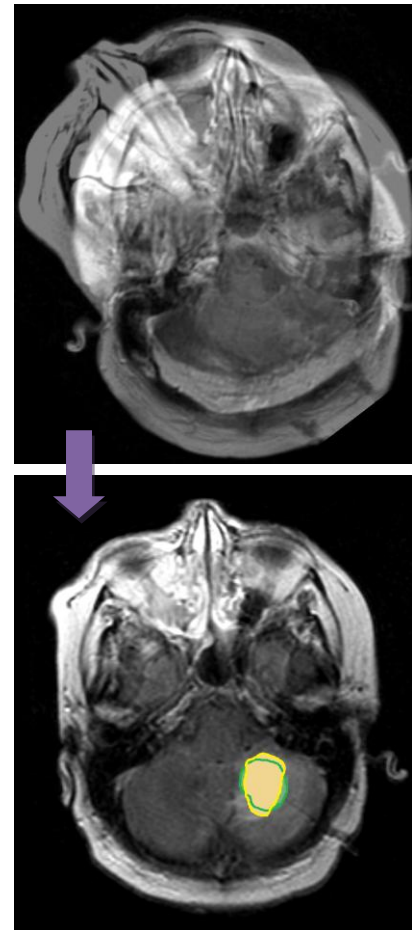


Fig 1. In the top figure, pre and post procedural images are shown before the registration demonstrating significant misalignment, while the bottom figure visualizes superimpose of the tumor (green) over the ablated zone (yellow) after the registration.

Low Intensity Focused Ultrasound Acoustic Characterization through Skull

Meghedi BABAKHANI* 1,2, Bryan NOWROOZI 1,2, George SADDIK 1,2, Ashkan MACCABI 1,2, and Warren GRUNDFEST 1,2,3.

1-Center for Advanced Surgical and Interventional Technology (CASIT), 2-Department of Bioengineering, 3-Department of Surgery, University of California, Los Angeles, CA USA;

Purpose: It has been demonstrated that Low Intensity Focused Ultrasound (LIFU) can be used to safely and reversibly target structures in the brain for neurostimulation purposes. Recent *in vivo* modulation of region-specific brain activity in mice suggests that LIFU may be a non-invasive, alternative therapy for drug-delivery applications and neurological diseases such as epilepsy and Parkinson's. For this technology to gain traction as a clinical therapy, further investigation of the targeting capabilities within the brain as well as the ultrasonic parameters that underlie LIFU-induced neurostimulation is required. Our research aims to characterize the precise energy deposition and beam deformation of LIFU application to improve our ability to compensate for the effects of the skull, and therefore enhance targeting during focused ultrasound mediated neurostimulation.

Methods: In preparation for *in vivo* LIFU efficacy studies, we examined beam deformation in *ex vivo* rat skulls, 2.8mm inferior from the bregma. We obtained beam patterns using a precision acoustic measurement tank, Olympus focused V301-SU transducer, and a precision hydrophone, targeting different regions of the brain. System parameters, including intensity attenuation, beam shape modulation, focal accuracy, and reverberation within the skull, were investigated.

Results: Preliminary data from ten rat skulls revealed that beam intensity, beam shape, and targeting are all significantly affected during transcranial sonication. These rat skull studies demonstrate that beam shape is substantially deformed by 2mm (Figure 1) in the sagittal plane and 0.5-1 mm shift in the transverse plane. This requires a minimum 4 mm target size in the sagittal direction for targeting purposes. Our studies also indicated that the beam focus heavily depends on the skull alignment with respect to the probe which is crucial during *in vivo* LIFU application. Changes due to beam deflection, internal reflection, reverberation, and attenuation must be taken into account to accurately target specific neuronal structures.

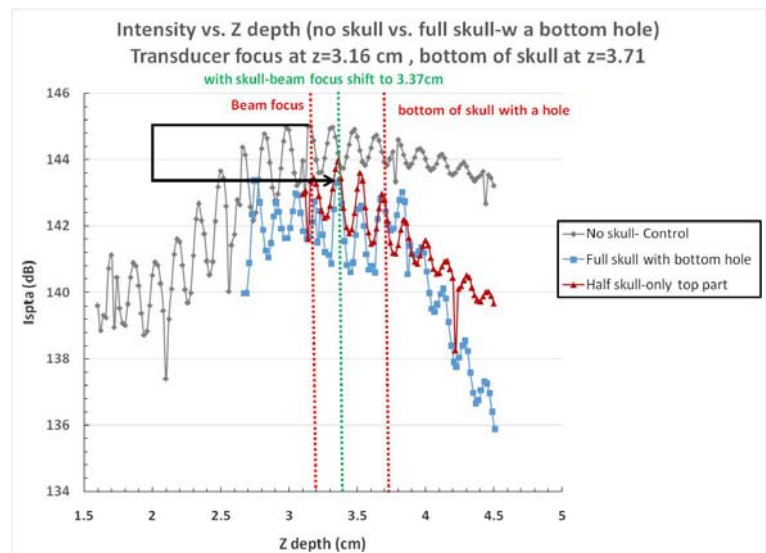


Figure 1: Beam reverberation, Intensity attenuation and targeting studies along the focus point, sagittal plane, with no skull vs. inside full skull where the hydrophone was entered through the bottom hole

Conclusions: This LIFU research supports ongoing efforts to characterize and understand beam propagation, deformation and targeting due to skull anatomy. This is a crucial first step in developing a potential new therapy for the treatment of brain diseases.

Development and Validation of an Endovascular Chemotherapy Filter Device for Removing High-Dose Doxorubicin from the Blood: *In Vivo* Porcine Study

Anand S. Patel, MD; Jeffrey Yang, BS; Maythem Saeed, DVM, PhD; Bradford Thorne; Prasheel Lillaney, PhD; Leo Sze, MS; Daniel L. Cooke, MD; Albert K. Chin, MD; Mark W. Wilson, MD; Steven W. Hetts, MD
Department of Radiology and Biomedical Imaging, University of California San Francisco

Purpose: A novel prototype disposable endovascular chemotherapy filter (CF) device was developed to remove excess doxorubicin (Dox) from the blood during intra-arterial chemotherapy (IAC) delivery to prevent systemic toxicities. Previous proof-of-concept established the capacity of the filter to bind Dox in swine serum *in vitro*. In this study, CF navigation, deployment and *in vivo* Dox binding was evaluated in the porcine inferior vena cava (IVC).

Materials and Methods: An 18 Fr CF device was constructed with an ion-exchange membrane attached to an expandable 28 mm diameter Nitinol frame (Fig 1B). Under X-ray fluoroscopy and contrast venography, the CF was percutaneously introduced via the internal jugular vein and deployed in the porcine infrarenal IVC (Fig 1A). 50 mg of Dox (2 mg/ml) was injected over 10 min in the IVC below the CF device. Venous catheters with tips proximal and distal to the CF device in the infrarenal IVC obtained pressures and blood samples for Dox concentrations over 90 min across the CF device membrane.

Results: The CF device was successfully introduced and deployed in the infrarenal IVC *in vivo*. Visualization under X-ray fluoroscopy verified the proper placement and mechanical expansion of the Nitinol framework. In a 90 min study, the device was biocompatible, not leading to hemodynamic disturbances: pressure measurements taken throughout the experiment yielded a maximum gradient of 17 mmHg across the CF membrane. Venography demonstrated non-flow-limiting thrombus associated with the CF device after 90 min of deployment (swine were not heparinized). Significant Dox binding was noted with an 85%, 74%, and 83% decrease in relative pre- versus post-filter Dox concentrations at times 3, 10, and 30 min, respectively after Dox injection (Fig 1C).

Conclusion: We developed a biocompatible CF device that can be safely introduced, deployed, and removed from the IVC *in vivo*. The CF device demonstrated significant Dox binding, and could serve as a platform technology in drug therapy to allow for higher regional doses of drug while limiting systemic toxicity. In future *in vivo* experiments, animals or the CF device itself will be heparinized in order to prevent thrombosis.

Reference: Patel A, Saeed M, Yee EJ, Yang JK, Lam G, Losey AD, Lillaney P, Thorne B, Chin A, Malik S, Chen C, Balsara N, Wilson M, Hetts SW. Development and Validation of Endovascular Chemotherapy Device for Removing High-Dose Doxorubicin: Preclinical Study. *J Medical Devices* (in press for 2014).

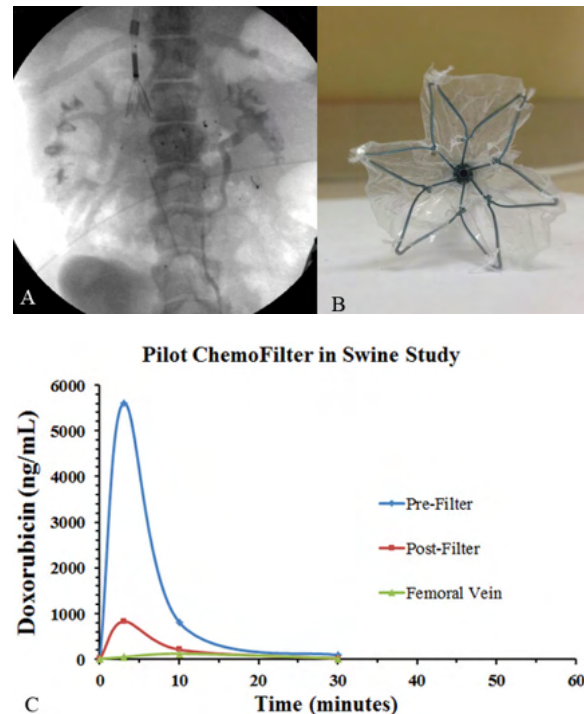


Figure 1. Catheter prototype with self-expanding nitinol tulip frame deployed in the IVC of a pig undergoing Dox infusion and filtration. (A) Fluoroscopic image of the swine demonstrating the ChemoFilter device in place with associated sampling catheters. (B) The expanded ChemoFilter device en-face. Notice nitinol cage with polymer resin membrane sutured onto the cage. (C) Dox concentration versus time with ChemoFilter in place during infusion of Dox in the infrarenal IVC. An 85% reduction in Dox concentration between pre-filter and post-filter samples at 3 minutes during peak infusion is consistent with Dox binding to the ChemoFilter.

Quantitative ultra-high resolution MR imaging using magnetic nanoparticles

Codi Amir Gharagouzloo^{1,2}, Srinivas Sridhar^{1,2}

¹ Nanomedicine Science and Technology Center, Northeastern University, Boston, MA

² Department of Bioengineering, Northeastern University, Boston, MA

Purpose

We resolved to create a non-destructive MRI modality to produce PET-like images, which would enable non-destructive image-guided therapy with high resolution. Typically, MRI signal is extremely difficult to quantify because of nonlinear artifacts resulting from magnetic susceptibility and flow/motion. Beyond physical signal interpretation limitations, the usage of the typical MR contrast agent (CA), gadolinium, is too toxic for theranostic applications. We thus chose iron-oxide nanoparticles as a CA because of their low toxicity profile.

Methods

We have developed a method deemed QUTE-CE (quantitative contrast-enhanced UTE) MRI utilizing a radial 3D ultra-short time-to-echo (UTE) pulse sequence to clearly delineate CA in positive-contrast images, and extrapolate concentration directly from those intensity measurements. Knowledge of CA relaxivity in whole blood along with a pre-calibration procedure allowed us to subsequently measure concentrations of ferumoxytol in mouse vasculature at 7T on a Bruker Biospec. QUTE-CE measurements were validated by analysis of iron content in blood draws following imaging sessions with inductively coupled atomic emission spectroscopy (ICP-AES).

Results

QUTE-CE MRI produced high resolution (150 μ m), positive contrast images of the FDA approved iron-oxide nanoparticle ferumoxytol (Feraheme®, AMAG Pharmaceuticals) in mouse vasculature. Pre-contrast images resulted in invisible organs (Fig. 1a) and post-contrast had 7% accuracy in vivo with a specificity of about 20nM of particles (Fig. 1b), or 6 μ g/ml elemental iron content. We demonstrated longitudinal measurements of CA and were able to display bioavailability and calculate CA half-life.

Conclusions

Our QUTE-CE method has unambiguously measured absolute concentration of iron-oxide CA directly from UTE intensity images at 7T. Future studies must be performed on clinical scanners, and the non-trivial step of quantification outside of the vasculature has yet been accomplished. QUTE-CE MRI enables quantitative imaging competitive with nuclear imaging albeit with high resolution.

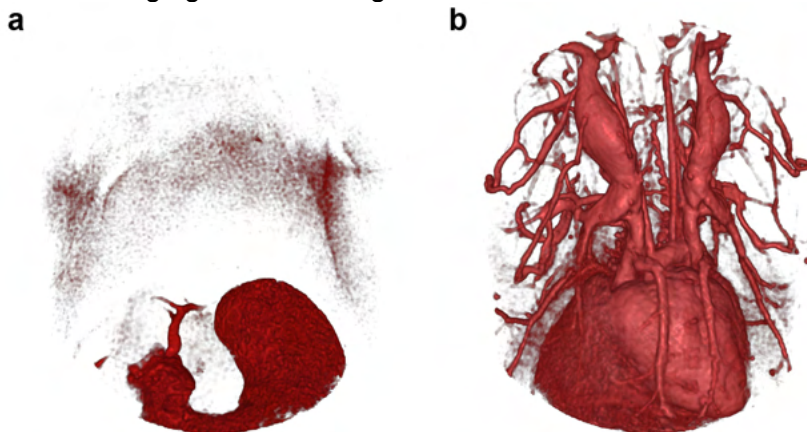


Figure 1. Demonstration of QUTE-CE in Thoracic Region of a Mouse. (a) Pre-contrast imaging renders organs and vasculature invisible and (b) post-contrast ferumoxytol renders vasculature.

Water Relaxation Parameters and the State of Protein Coagulation in Vascular Repair by MR Coagulation

Ming Zhao,^{1,2} Jerome L. Ackerman^{1,2,3}

¹Physics Department, University of Massachusetts Lowell, Lowell, MA;

²Martinos Center, Department of Radiology, Massachusetts General Hospital, Charlestown, MA;

³Harvard Medical School, Boston, MA

Purpose: To measure the MR relaxation properties of a protein solution undergoing coagulation to determine the most definitive MR methodology enabling the detection of coagulation. Coagulation of a protein biomaterial by MR-induced RF heating is a novel means to effect repair of vascular defects such as aneurysms or arteriovenous malformations. These defects are conventionally repaired by surgical clipping or by filling/occluding with endovascularly delivered wire coils, and in some cases with particles or a polymeric material. Our novel method, MR Coagulation, is intended to achieve a comparable result by coagulating a thermosetting biomaterial (such as a protein solution) delivered endovascularly by catheter and coagulated by RF-induced heating of an intracatheter resonant wire antenna in the MRI scanner. In an image guided MR coagulation procedure it is necessary to establish the rheological state of the biomaterial and to determine when coagulation is complete using its MR characteristics. Egg white, essentially a 20 wt% protein solution with about half the protein being ovalbumin, can be used as an inexpensive substitute for HSA for investigating heat coagulation behavior and MR relaxation properties. In this study, the MR relaxation properties of egg white were studied as a function of temperature and degree of coagulation to determine which relaxation time constants would be most appropriate for future imaging studies to ascertain the coagulation state in vivo.

Methods: Proton spectra of the water signal in egg white were obtained at 14 T at an increasing series of temperatures from 20 to 70 °C with inversion recovery, CPMG or spinlock preparation to measure the water spin-lattice relaxation time T_1 , spin-spin relaxation time T_2 , or rotating frame spin-lattice relaxation time $T_{1\rho}$ respectively. A parallel study utilized light scattering at 617 nm to establish the degree of coagulation by an independent method.

Results: It was found that water T_2 and $T_{1\rho}$ gave the most definitive indication of the change from uncoagulated at low temperature to fully coagulated at 60 °C, while water T_1 showed only the expected increase with temperature, and no response to coagulation. The optical absorbance vs. temperature curve showed a definitive transition from uncoagulated to coagulated state over the same temperature interval as did T_2 and $T_{1\rho}$.

Conclusion: The NMR and light scattering experiments show that egg white protein fully coagulates at 60°C, which is relatively easy to achieve by MR-induced heating of an intracatheter antenna. T_2 weighted imaging is expected to be the optimum method to establish the coagulation condition of the biomaterial.

Funding: Support was provided by University of Massachusetts Lowell, Center for the Integration of Medicine and Innovative Technology (CIMIT) grant 13-1180/grant W81XWH-09-2-001 from U.S. Army Medical Research and Materiel Command (USAMRMC), NIH grants RR023009 and P41RR14075, and the Athinoula A. Martinos Center for Biomedical Imaging.

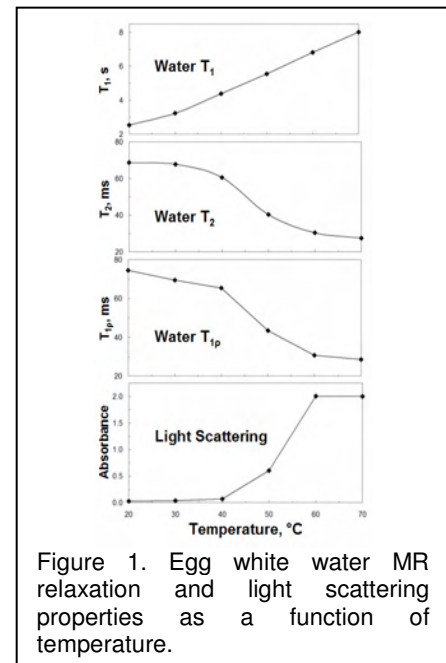


Figure 1. Egg white water MR relaxation and light scattering properties as a function of temperature.

Rapid Segmentation of the Median Nerve for a Video-Guided Ultrasound System

Aaron Sun¹, Vikas Shivaprabhu¹, Jihang Wang¹, John Galeotti^{1,3},
Vijay Gorantla², George Stetten^{1,3}

Departments of Bioengineering¹ and Reconstructive Surgery², University of Pittsburgh
Robotics Institute, Carnegie Mellon University³

Purpose

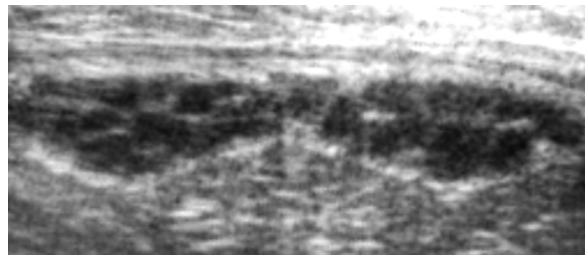
We seek to provide a rapid yet effective method towards segmentation that lends itself to parallelization through GPU technology. In this particular application, the target is identification of fascicles in 2D and 3D high resolution ultrasound scans (HRUS) of the median nerve at 50 MHz as part of a new system combining video from a probe-mounted camera with ultrasound data to monitor the progression of blood vessels and nerves after reconstructive surgery.

Methods

The method involves three parts: formation of pixel clusters (*patches*), identification of boundary points and medial points, and segmentation by grouping. We begin by constructing patches of homogeneous pixels using a directed graph of edges between neighboring pixels in order to reduce noise and subsequent computational cost while preserving meaningful structures. Pixel intensity as well as variance are factored into a descending variance graph, where the variance and mean are calculated within a sphere of radius r centered at the pixel. Each pixel points to the neighbor with the lowest magnitude of the ratio of difference in intensity to difference in variance, and the pixels in the corresponding disjoint trees set their intensities to the mean of the root pixel. Next, each patch finds the point where a line drawn between its root and the root of a bordering patch intersects the boundary between them (the *boundary point*). Given the set of all boundary points, we find *medial points* that lie equidistant from any two boundary points within a desired range of distances. For these medial points to form, the patches that the lines between the medial point and its two boundary points intersect must also meet a minimum threshold for homogeneity. Thus, medial points are a measure of association: the more medial points formed by the same pair of boundary points, the stronger the association between those boundary points. Utilizing this, boundary points are clustered into mutually exclusive *boundary point sets* by linking each boundary point with its highest N associated boundary points, where N is user-defined (in our case, 5). The final step involves matching patches to boundary point sets by having each medial point within a patch vote for a boundary point set only if that set contains both of the boundary points associated with that medial point.

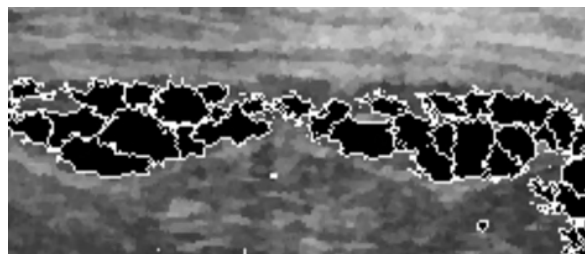
Results

Segmentation of the median nerve imaged at 50 MHz was performed using 2D data (< 1 second) and reconstructed 3D data (< 7 seconds) with image sizes of 256x256 and 256x256x18. Results of a slice from the latter are shown to the right. Fascicles are identified despite noise in the original image and incomplete boundaries.



Conclusions

Our method shows effective segmentation of the median nerve in 2D and 3D in HRUS ultrasound data, with rapid computation times due to GPU implementation. Further optimization and development of these routines hold promise for our application of combining ultrasound analysis and video navigation in real time.



Assessment of *In vivo* Corneal Hydration Using Terahertz Imaging

Shijun Sung¹, Neha Bajwa², James Garritano², David Bennett¹, Bryan Nowroozi^{2,3}, Jean-Pierre Hubschman⁴, Sophie Deng⁴, Warren Grundfest^{1,2,3}, Zachary Taylor^{2,3}

¹ Department of Electrical Engineering, University of California (UCLA), Los Angeles, CA

² Department of Bioengineering, UCLA

³ Department of Surgery, UCLA David Geffen School of Medicine

⁴ Jules Stein Eye Institute, UCLA

Purpose: Accurate and practical imaging techniques for *in vivo* ocular hydration remain elusive. We report terahertz and millimeter wave reflection-mode imaging of corneal hydration that directly resolves spatial and temporal hydration gradients in the cornea, an important indicator of ocular health. This imaging technique is aimed to detect characteristic abnormal hydration levels in conditions such as Fuchs' dystrophy, corneal graft rejection, and membrane malfunctions. THz imaging provides a direct method to measure hydration.

Methods: THz reflection images of *in vivo* rabbit cornea are acquired using two center wavelengths at 100GHz and 525GHz (Figure 2). Wavelength choice in this regime affects hydration sensitivity, depth of penetration, and imaging parameters such as resolution and depth-of-focus. At 100GHz, focused THz illumination of 3mm diameter allows for point-measurement of the cornea's THz reflectivity. At 525GHz, images of the cornea are acquired with a focused spot size of 0.8mm. THz signal is taken in conjunction with a corneal thickness measurement using ultrasound pachymetry. Corneal hydration of an anesthetized, pain-managed rabbit is modulated with the application of tear drops and gentle dry wind. THz images are acquired immediately after varying hydration.

Results: THz images at 525GHz show contrast that is generated by the hydration profile across the cornea (Figure 3). At both 100GHz and 525GHz, changes in THz reflectivity are observed when the corneal hydration is varied within the physiological range (78-81%). Electromagnetic modeling suggests that a longer wavelength choice provides higher sensitivity to changes in hydration, while shorter wavelengths more accurately probe the stroma for accurate hydration measurement. THz imaging techniques directly measure corneal hydration and provide clear advantages over the current clinical method of corneal hydration measurement which use ultrasound pachymetry to correlate corneal thickness to hydration.

Conclusions: THz imaging demonstrates changes in reflectivity in cornea due to hydration content, offering a direct measurement method of corneal hydration for ophthalmologic assessment.

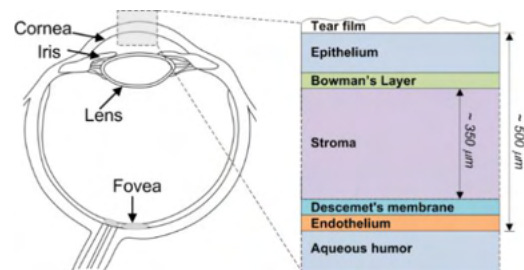


Figure 1. Ocular anatomy and cornea structure. Hydration is modulated in the bulk of body in the Stroma

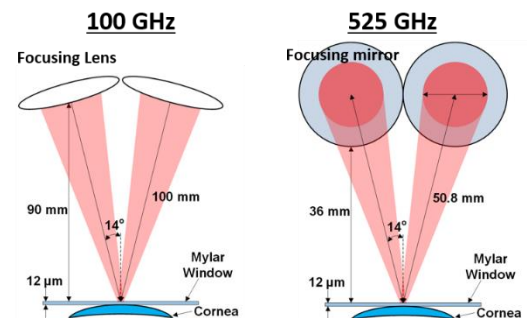


Figure 2. Imaging set-up for cornea.

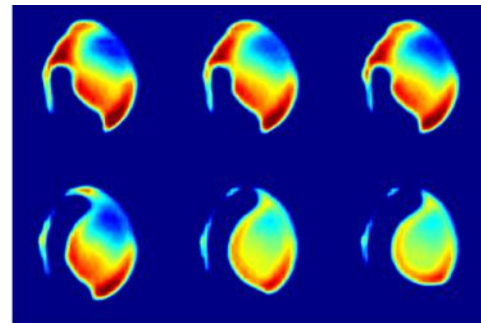


Figure 3. THz images of *in-vivo* cornea at 525GHz. Images are arranged from the most hydrated to least hydrated. THz images show contrast within each images indicating hydration profile changes across the cornea.

Implementation of gesture control concepts for data accessibility in intraoperative settings

Franklin King¹, Saskia M. Camps², Andras Lasso¹, Tobias Penzkofer², Steve Pieper^{2,3}, Tina Kapur², and Gabor Fichtinger¹

¹ Laboratory for Percutaneous Surgery, School of Computing, Queen's University, Kingston, Canada

² Surgical Planning Laboratory, Department of Radiology, Brigham and Women's Hospital, 75 Francis St, Boston, USA

³ Isomics Inc., 55 Kirkland Street, Cambridge, MA, USA

Purpose: The success of integrating state-of-the-art technologies for medical image-guided procedures has developed a need for interfaces to manipulate data. Commonly used control devices, such as keyboard and mouse, prove to be problematic in intraoperative settings, often requiring assistance from those other than the clinician or are otherwise inconvenient. Touchless gesture-based controls offer a potential interface that may alleviate these issues. Emerging hand and finger tracking devices such as the Leap Motion controller may be suitable for this purpose. We aim to implement a touchless interface prototype using the Leap Motion controller in order to explore methods in which to achieve a precise and intuitive interface thereby satisfying prerequisites for intraoperative use.

Methods: Prototype interfaces were implemented for the medical image framework 3D Slicer (www.slicer.org). Multiple sets of gesture control concepts were mapped to actions such as slice selection, window and level adjustments, and rotation of 3D objects. Focus was laid upon using well-performing gestures for a limited set of actions.

Results/Discussion: One recurring issue that was encountered during creation of the prototype interfaces was the recognition of unintended gestures. It was therefore necessary to implement systems for activation and deactivation. Different menu systems were developed to address this situational unreliability of the Leap Motion controller's accuracy (Figure 1). The menu systems allowed for the usage of a limited set of well performing gestures to be used for multiple actions. In the current implementation this is done by using the specific gestures supported by the Leap Motion API. There is, however, a tradeoff between gestures that are easy to accomplish and learn, and gestures that are less likely to be the result of unintended actions. Another concern was fatigue after extended use, necessitating actions to be completed within a reasonable time frame with hands placed at a comfortable position for the clinician. As the Leap Motion controller only scans a limited area above the device, small hand actions are sufficient to perform different actions. These might be more convenient in an intraoperative setting compared to, for example, a Kinect implementation in which large arm motions are required.

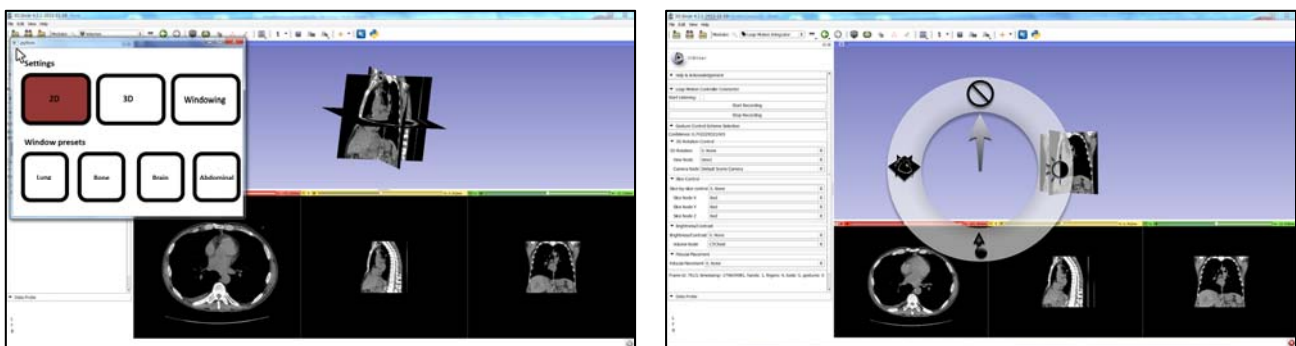


Figure 1: Cursor based (left) and radial (right) menu system implementations for Leap Motion controller use with 3D Slicer

Conclusion: Touchless interface prototypes were successfully developed using multiple gesture concepts. Future implementations can be improved by adding visual, audio, or physical user feedback.

Acknowledgements: This work was in part funded by Cancer Care Ontario through Applied Cancer Research Unit and Research Chair in Cancer Imaging grants. This work was also partly supported by a research agreement between Siemens Healthcare (SY) and Brigham and Women's Hospital, as well as NIH grants P41EB015898 and P41EB015902.

Usability Evaluation of a Touchless User Interface for 3D Slicer

Saskia M. Camps¹, Franklin King², Andras Lasso², Steve Pieper^{1,3}, Tina Kapur¹, Gabor Fichtinger² and Tobias Penzkofer¹

¹ Surgical Planning Laboratory, Department of Radiology, Brigham and Women's Hospital, 75 Francis St, Boston, USA ² Laboratory for Percutaneous Surgery, School of Computing, Queen's University, Kingston, Canada ³ Isomics Inc., 55 Kirkland Street, Cambridge, MA, USA

Purpose: Navigating and controlling the presentation of pre-operative multi-modality imaging information during interventions is challenging, due to the sterility requirements and limited available workspace. In many cases the task is accomplished using voice commands through another person, which is prone to error and can be time-consuming. Touchless gesture-based controls offer a solution for this issue by returning the control to the person performing the procedure. In this study we used an infrared light based controller which is capable of real time tracking of hands and fingers. Since there are many different ways to implement a user interface based on this controller architecture, goal of this study was to evaluate the user experience for a particular implementation of such a system.

Materials and Methods: A menu-based interface using the Leap Motion controller (Leap Motion, San Francisco, CA, USA) was implemented for the open-source medical imaging framework 3D Slicer (www.slicer.org), see also [1]. The user is able to select a specific function by pointing on a menu window (Figure 1), which is subsequently triggered by hand movements (rotational and up-down). 5 subjects performed a set of 6 tasks (3 times slice selection, 3 times window/brightness adjustment) in a randomized order, after 10 minutes training with the system. Time to complete the tasks was measured as an objective parameter, the NASA Task Load Index [2] and System Usability Scale [3] questionnaires were used as subjective

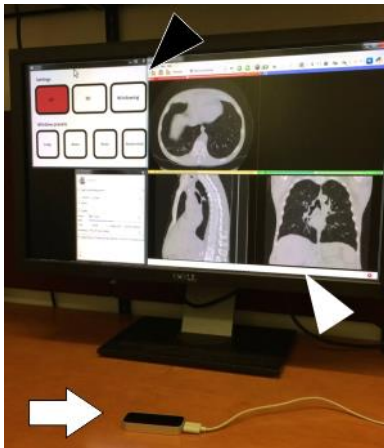


Figure 2: Leap Motion setup: Menu (black arrowhead), Slicer window (white arrowhead), Leap Motion controller (white arrow).

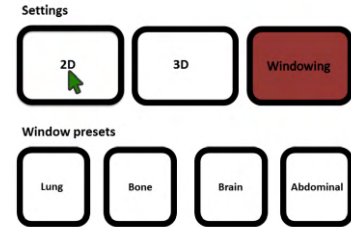


Figure 1: Menu for function selection. The cursor is controlled with the Leap Motion controller in the XY plane. If a user stays at a certain position the cursor turns gradually from white to green until the underlying button is activated. In this case, the green cursor signifies that the 2D scroll function is about to be selected.

measures for task demand and perceived usability, respectively. **Results/Discussion:** The tasks were completed in on average $72.7 \pm 69.5s$ ($\pm SD$). The variation can be attributed to the level difference of the users: Novice users (users who never were exposed to the Leap Motion controller) needed on average $95.2 \pm 81.9s$, users with previous experience with the controller only $39.1 \pm 18.5s$ ($p=0.0279$). No significant difference could be found ($p=0.33$) between the time required to perform the two tasks, slice selection ($60.1 \pm 44.1s$) and window setting ($85.3 \pm 88.03s$). The performance dimension in the NASA TLX questionnaire (1-21 points scale, 1 better than 21) was 5.2 ± 3.7 for the window selection and 3.4 ± 1.9 for slice selection ($p=0.403$), the ease of use dimension of the System Usability Scale (5 point Likert scale) was 3.0 ± 1.22 for windowing and 3.2 ± 0.58 for slice selection ($p=0.83$).

Conclusion: The system was tested in a mixed group of novice and advanced users of the controller. A difference between novice and experienced users indicates a strong relevance of training and

should be emphasized upon introduction of such a system.

Acknowledgements: This work was partly supported by a research agreement between Siemens Healthcare (SY) and Brigham and Women's Hospital, as well as NIH grant P41EB015898 and P41EB015902. This work was also in part funded by Cancer Care Ontario through Applied Cancer Research Unit and Research Chair in Cancer Imaging grants. **References:** 1. King et al., Implementation of gesture control concepts for data accessibility in intraoperative settings, NCIGT Workshop 2014, Boston, USA 2. Hart, S., & Staveland, L. (1988). Development of NASA-TLX (Task Load Index): Results of empirical and theoretical research. In P. Hancock & N. Meshkati (Eds.), Human mental workload (pp. 139-183), Amsterdam. 3. Brooke, J. (1996). "SUS: a "quick and dirty" usability scale". In P. W. Jordan, B. Thomas, B. A. Weerdmeester, & A. L. McClelland. Usability Evaluation in Industry. London: Taylor and Francis

Feasibility of intraoperative imaging with reflectance confocal microscopy to potentially guide Mohs surgery

Eileen S. Flores, Miguel Cordova, Kivanc Kose, William Phillips, Anthony Rossi,
Kishwer Nehal, Milind Rajadhyaksha

Dermatology Service, Memorial Sloan Kettering Cancer Center, New York, NY, USA

PURPOSE

Mohs surgery for the removal of non-melanoma skin cancers (NMSCs) is performed in stages, while being guided by the examination for residual tumor with frozen pathology. However, preparation of frozen pathology at each stage is time-consuming and labor-intensive. Reflectance confocal microscopy (RCM) can be utilized to detect lateral tumor margins, assess margin status in ex-vivo Mohs specimen layers, and assess the base of Mohs surgical wounds for residual tumor. Our study tests feasibility of real-time intraoperative RCM for rapid detection of residual tumor directly in surgical wounds on Mohs patients.

METHODS

We report initial results on twenty-five patients, who presented with superficial surgical wounds at the MSKCC Dermatology service. RCM imaging, using 35% AlCl_3 for nuclear contrast, was performed with the Vivascope 3000 (Caliber ID). Imaging was performed in quadrants in the wound, to simulate the Mohs surgeon's examination of pathology. Images and videos were taken at the epidermal and deep dermal margins. Mohs surgeon assessed all images, videos and video-mosaics for quality and correlation to histology.

RESULTS:

RCM images, videos, and video-mosaics of the epidermal and dermal margins were found to be of clinically acceptable quality. Bright nuclear morphology was identified at the epidermal margin. The presence of residual BCC/SCC tumor and normal skin features could be detected in the peripheral and deep dermal margins. Nuclear morphology was detectable in residual BCC/SCC tumors. RCM and histopathological correlation was seen in a majority of the wounds.

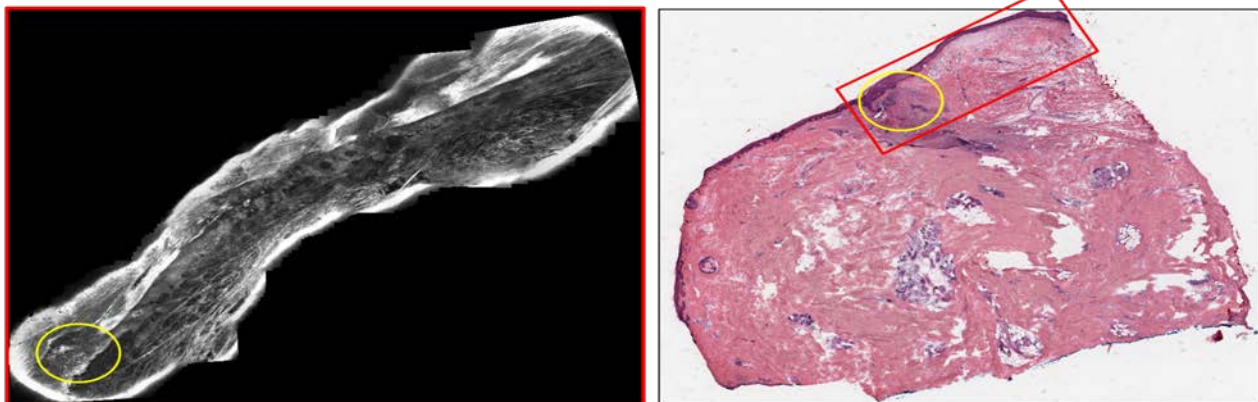


Figure 1. Intraoperative RCM imaging and histology confirmation of residual superficial BCC

CONCLUSIONS

Intraoperative RCM imaging may enable detection of residual tumor, directly on Mohs patients, and may serve as an adjunct for frozen pathology. However, a stronger source of contrast will be necessary, and also a smaller device with an automated approach for imaging in the entire wound in a rapid and controlled manner for clinical utility.

Electromagnetic Tracking for Catheter Path Reconstruction

Elodie Lugez, Hossein Sadjadi, Selim G. Akl, Gabor Fichtinger
School of Computing, Queen's University, Kingston, ON

Purpose: Accurate catheter tracking is required for various procedures such as high dose rate (HDR) prostate brachytherapy, where catheter path reconstruction is a necessary step to optimize the position of the radioactive source and the dwell times. Electromagnetic (EM) tracking has been introduced in order to overcome the limitations of path reconstruction using standard imaging modalities [1]. However, EM measurements are noisy and subject to distortion in clinical settings. While several error minimization techniques have been proposed, the tracking error still poses a challenge in accurate path reconstruction. In this study, we propose to tackle this challenge by introducing a novel filtering technique that incorporates the nonholonomic motion constraints of the EM sensor in the catheter path.

Methods: The motion of the sensor in the catheter is nonholonomic, as the sensor is assumed to move along the catheter path [2]. We employ a Kalman filter (KF) to integrate the nonholonomic motion of the EM sensor with the raw measurement data. We have experimentally evaluated the performance of our proposed approach using an Ascension trakSTAR (Ascension Tech. Corp., Milton, VT) and a 6 degrees of freedom (model 55) sensor. A 3D printed calibration phantom firmly held 30 cm long catheters into predefined ground truth paths. The experimental setup was placed in an environment with field distorting objects resembling clinical interferences. The EM sensor measurements were recorded while it was inserted and retracted into the path. We collected raw measurement data and applied our method to improve the tracking performance. We compared our results with the filtered data provided by the manufacturer.

Results: For the raw measurement data, the root-mean-square (RMS) error along the path was 5.6 mm, and was 2.4 mm with filters provided by the manufacturer. Using the KF with the nonholonomic motion model, the RMS was reduced to 1.8 mm, as tabulated in Table 1.

Table 1. Path reconstruction accuracy

	Raw measurements	Standard manufacturer filter	Nonholonomic Kalman filter
Minimum error	0.0 mm	0.1 mm	0.0 mm
Maximum error	23.4 mm	7.0 mm	5.8 mm
RMS error	5.6 mm	2.4 mm	1.8 mm

Conclusions: Compared to other filtering methods, our approach has the advantage of exploiting the additional orientation measurements in its formulation. This information combined with the position measurements can successfully improve the accuracy of path reconstruction. In conclusion, filtering using a nonholonomic model is promising for clinical procedures requiring the reconstruction of catheter path such as HDR brachytherapy.

References:

- [1] Zhou, Jun, et al. Real-time catheter tracking for high-dose-rate prostate brachytherapy using an electromagnetic 3D-guidance device: A preliminary performance study. *Med. Phys.* 40.2 (2013): 021716.
- [2] Duindam, Vincent, et al. Three-dimensional motion planning algorithms for steerable needles using inverse kinematics. *The International Journal of Robotics Research* 29.7 (2010): 789-800.

Acknowledgements: Elodie Lugez was supported by the Natural Sciences and Engineering Research Council of Canada. Gabor Fichtinger was supported as Cancer Care Ontario Research Chair.

Effect of Data Acquisition Speed and Technique on the Identification of Brachytherapy Source Positions with an Electromagnetic Tracker

Sarah M. Don, Robert A. Cormack, Akila N. Viswanathan, and Antonio L. Damato

Department of Radiation Oncology, Brigham and Women's Hospital and Dana-Farber Cancer Institute, Boston, MA

Purpose: Image guidance is widely used in gynecologic brachytherapy procedures, but challenges remain in the correct identification of possible source positions (dwells) inside the brachytherapy catheters inserted into the tumor. The use of electromagnetic (EM) tracking has been recently explored (1-3) as a possible complement to CT and MR guidance. The purpose of this study was to measure the error in dwell identification using different EM positional data acquisition techniques, environmental conditions, and data collection speed.

Methods: An Ascension TrakSTAR EM tracker system was used to obtain positional data of catheters in a phantom implanted with 9 brachytherapy catheters. Two acquisition techniques were considered: continuous and stepwise. Continuous acquisition was performed by withdrawing the sensor from the catheter by hand. The experiment was repeated at 3 different speeds in two environmental conditions: ideal (no metallic distortion) and clinical (some metallic distortion). Stepwise acquisition (1) was performed by acquiring data for 30 seconds at evenly-spaced positions, with different speeds simulated by randomly sampling shorter acquisition times. The dwell error (maximum distance between any EM-identified dwells and the dwells identified manually on CT as per clinical practice) and the catheter error (average of the average distance of all the dwells in a catheter) were calculated.

Results: Errors < 2 mm were observed for all acquisition techniques in ideal conditions when the data collection time per catheter was > 10 seconds. Errors < 4 mm were observed for clinical conditions. The data suggests that a stepwise acquisition with dwell duration < 10 seconds per catheter with error < 2mm is possible. Results are shown in Figure 1 and 2.

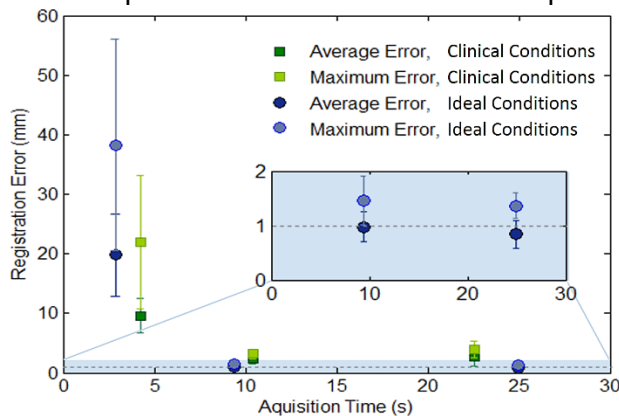


Figure 1 – Average and maximum errors for continuous acquisitions with three different speeds and two different noise levels, averaged over 9 catheters.

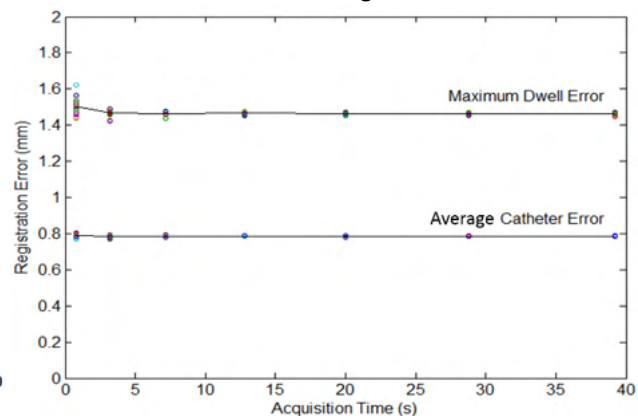


Figure 2 – Average and maximum errors for stepwise acquisitions with 7 different dwell durations in ideal environmental conditions.

Conclusions: Continuous acquisition can be used for acquisition times of > 10 seconds per catheter. For brachytherapy treatments with a large number of catheters needing a faster acquisition, a stepwise acquisition may be warranted. Additional experiments will be performed to validate this result.

Funding Sources: Kaye Family Award

References: 1. Damato A, Bhagwat M, Buzurovic I, *et al. Medical Physics* 2014;41:487-488.; 2. Damato A, Mehrtash A, Kapur T, *et al. Medical Physics* 2013;40:103-104. 3. Mehrtash A, Damato A, Pernelle G, *et al. SPIE Medical Imaging: International Society for Optics and Photonics*; 2014. pp. 90361F-90361F-90368.

Bi-exponential diffusion analysis in normal prostate and prostate cancer: transition vs peripheral zone considerations

Thiele Kobus¹ – Andriy Fedorov¹ – Fiona Fennessy² - Robert Mulkern³ - Clare Tempany¹ – Stephan Maier¹

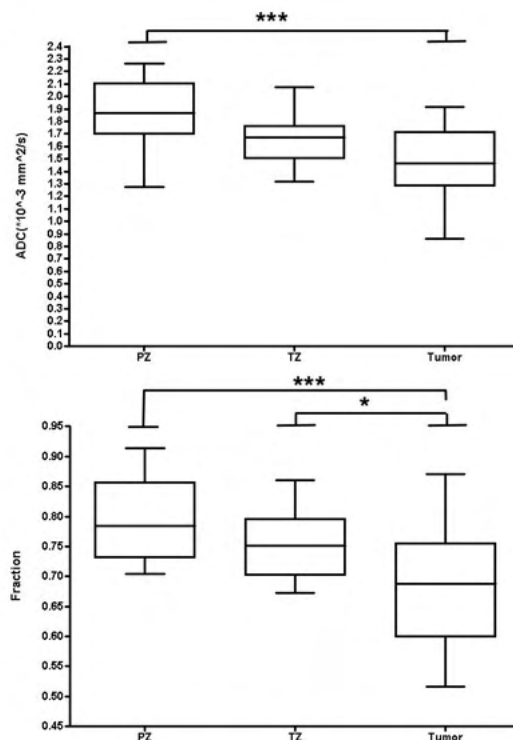
¹ Department of Radiology, Brigham and Women's Hospital, Boston, ² Department of Radiology, Dana-Farber Cancer Institute, Boston, ³ Department of Radiology, Boston Children's Hospital, Boston

Purpose: Prostate diffusion-weighted imaging (DWI) is typically performed using a small number of b-values under 1000s/mm² with apparent diffusion coefficients (ADC's) calculated assuming mono-exponential decays. Over an extended range of b-values, bi-exponential fits better characterize the signal decay and offer additional tissue characterization, which may serve to differentiate transition zone (TZ) tumors from normal tissue (Liu et al MRI 2013). Here, the value of bi-exponential tissue parameterization for tumor differentiation in both the TZ and peripheral zone (PZ) is examined.

Materials and methods: In this IRB approved study, 19 patients had a multi-parametric endorectal prostate MR exam at 3T. Conventional DWI (b=0 and 500s/mm², TE 72ms) and multi-b DWI (15 b-values from b=0 to 3500s/mm², TE 102ms) were performed with diffusion sensitizing gradients along 3 orthogonal directions. ADC maps were generated using scanner software for clinical DWI, and a custom tool in 3D Slicer for multi-b DWI to determine ADC-fast, ADC-slow and fast diffusion fraction. Two readers assigned in consensus on b0 images, guided by T2w images, the following regions: normal appearing PZ, normal appearing TZ and suspected tumor (in PZ and TZ). Readers were blinded to conventional ADC maps but allowed to consult T1w images to rule out blood. For all regions the mean values were determined. ANOVA analysis was used to compare the three tissues.

Results: Ten tumor suspicious regions were located in the PZ and 8 in the TZ. Significant differences between PZ and tumor tissue ($p < 0.001$) and between TZ and tumor tissue ($p < 0.05$) were observed for the fast diffusion fraction. From the ADC of b500-DWI, a significant difference was only observed between PZ and tumor tissue ($p < 0.001$). No significant difference was observed for ADC-fast and ADC-slow among different tissues.

Conclusion: The fast diffusion fraction allows for better tumor discrimination than the b500-ADC values extracted in this study even in the TZ. The observed change in mono-exponential based ADC values stems from a decrease in the fast diffusion fraction with ADC-slow and ADC-fast values exhibiting only small variations.



Quantitative and volumetric analysis of prostate cancer using mpMRI: a comparison of whole mount pathology images versus routine pathology reports

A. Fedorov, T. Penzkofer, M. Vangel, M.S. Hirsch, C.M. Tempany-Afdhal, F.M. Fennessy
Brigham and Women's Hospital, Boston, MA

Purpose To compare two methods of pathological validation of multiparametric MRI (mpMRI) for prostate cancer (PCa) detection, tumor volumetric assessment, and quantitative differentiation of PCa from non-neoplastic tissue (NNT).

Methods Patients with known PCa and endorectal 3T mpMRI were prospectively consented for whole mount pathology (WMP) processing of their prostate. mpMRI included T1 and T2-weighted, diffusion weighted ($b=500$) and dynamic contrast enhanced (DCE) MRI. Significant PCa foci (SPCa) ($\geq 0.5\text{cc}$) were outlined on WMP slides. SPCa in the peripheral zone (PZ) and NNT were segmented on T2, ADC and DCE by a radiologist on 2 occasions: using side-by-side digitized WMP slides, and 6 months later using only the final surgical pathology reports (SPR) and blinded to the WMP. Agreement in WMP/SPR lesion locations was assessed based on prostate zonal anatomy. Linear discriminant analysis (LDA) of ADC and pharmacokinetic parameter K_{trans} was used to evaluate the discriminating power of separating SPCa and NNT. Spatial overlap between the WMP and SPR based contours was assessed with Dice similarity coefficient (DSC). SPCa volumes were compared using paired t-test.

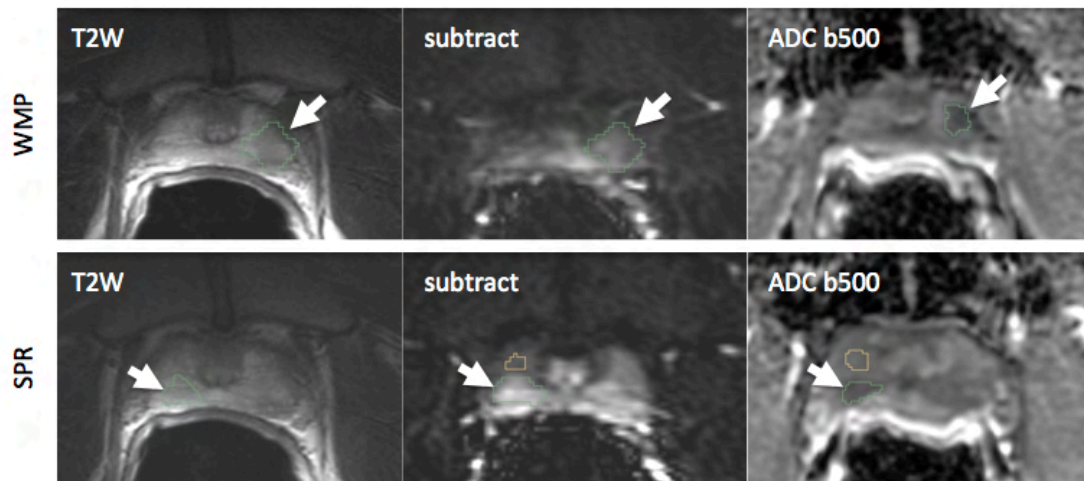


Fig.1: Illustrative example of discordant localization of the SPCa, where WMP was necessary to accurately identify the SPCa. Top: SPCa localization using whole mount annotations as the reference; the SPCa chosen was identified on the left of the patient's prostate, as defined from WMP. Bottom: SPCa localization using SPR, however, chose a suspicious-appearing lesion on the right as the SPCa (outlined in green). (Note normal peripheral zone is outlined in yellow on the same slide in this case).

Results Out of 30 patients enrolled, 14 were excluded due to hemorrhage, no tumor in PZ, or tumor $< 0.5\text{cc}$. SPCa's were present in 16 cases based on WMP. Gleason score was ≥ 7 in 15/16 cases; a Gleason score was not assigned in the last case due to neoadjuvant hormonal treatment. In all 16 cases SPCa's were also identified using SPR. Anatomical locations of the SPCa's identified using WMP and SPR agreed in 13/16 cases. In the remaining 3 cases there was a mismatch in the lesion location between WMP- and SPR-based approaches. WMP/SPR DSC were (mean \pm SD): T₂ 0.62 \pm 0.22; DCE 0.63 \pm 0.13; ADC 0.6 \pm 0.17. LDA analysis of K_{trans} and ADC did not demonstrate a difference between WMP and RPT in separating SPCa from NNPT. There was no significant difference in SPCa volumes outlined by WMP and SPR.

Conclusions WMP was better for accurate SPCa localization in 3/16 patients. In 13 SPCa's identified by mpMRI concordantly with RPT, there was no significant difference in the size of tumor, or discriminating power of mpMRI parameters between the WMP and SPR approaches. Overall, correlation of mpMRI of prostate with a detailed pathology SPR or with digitized WMP images provided similar quantitative and volumetric mpMRI analyses of the correctly localized focal lesions.

Acknowledgments This work was supported by NIH U01 CA151261. TP received a grant from RWTH Aachen University Hospital.

Clinical Application of 4-DOF Needle Guiding Manipulator for MRI-guided Transperineal Prostate Biopsy

Tokuda J¹, Tuncali K¹, Eslami S², Shang W³, Li G³, Patel N³, Heffter T⁴, Fischer GS³, Iordachita I², Burdette EC⁴, Hata N¹, Tempny CM¹

¹Brigham and Women's Hospital, Boston, MA, ²Johns Hopkins University, Baltimore, MD, ³Worcester Polytechnic Institute, Worcester, MA, ⁴Acoustic MedSystems Inc., Savoy, IL

Introduction. Prostate cancer (PCa) is the most common cancer among men in the U.S. accounting for about 29,480 deaths annually [1]. While transrectal ultrasound (TRUS)-guided systematic biopsy is the most common approach to definitive diagnosis, its limited negative predictive value has been argued [2,3]. MRI has been widely accepted for localization of PCa [4], and investigated as a modality to guide targeted biopsy [5,6]. To place a biopsy needle accurately at designated location under MRI-guidance, we developed a 4 degrees-of-freedom (DOF) MRI-compatible needle guiding manipulator [7] and tested in MRI-compatible transperineal biopsies of two patients with suspected PCa.

Methods. Biopsies were performed in a wide-bore 3T MRI (IMRIS, Inc.). The manipulator was composed of 2 similar front and rear trapezoid stages driven by four MRI-compatible piezoelectric motors. The manipulator was equipped with a platform to guide a needle. **Patient setup:** A patient was placed on the table in the lithotomy position. After the skin around the perineum was cleaned, a stabilizing frame, which held the patient thighs to secure the workspace near the perineum, was fixed on the table. The frame had an embedded Z-frame, an MR-visible frame to register the manipulator to the image coordinate system. After a body matrix coil (Siemens AG) was placed, the manipulator was docked on the patient table (Fig. 1A).

Planning: MR images of the Z-frame (Z-frame image) and the prostate (planning image) were acquired using a T2-weighted multislice turbo spin echo sequence. The images were loaded onto RadVision software (Acoustic MedSystems, Inc.) and 3D Slicer software [8]. The RadVision software computed the transformation matrix between the image and manipulator coordinate systems using the Z-frame image. On the 3D Slicer software, biopsy targets were defined on a preoperative MRI, and mapped onto the planning image using deformable image registration [9]. 3D Slicer exported the mapped targets to RadVision. **Targeting:** The target coordinates were transferred to the manipulator over the network using OpenIGTLink [10]. The manipulator then positioned the needle guide platform to direct the needle to the target. A radiologist inserted a biopsy needle (InVivo) manually along the guide using a specified needle insertion depth (Fig. 1B). The needle was confirmed by a newly acquired T2-weighted image.

Results. In the two clinical cases, tissues were sampled from 3 and 1 locations successfully with total operation times of 71 minutes and 54 minutes (from the first scan to the last scan) respectively. The root mean square errors between the planned target and the needle path on MR images in the first attempt for each target were 3.7 mm and 9.4 mm respectively. In the second case, the needle path was deviated from the planned path due to bending of the needle at the first attempt, but corrected in the successive needle insertion.

Discussion. This pilot study demonstrated that the new manipulator was feasible to be used in MRI-guided transperineal biopsy. In this study, we kept the needle insertion path parallel to the static magnetic field for the simplicity, although the mechanism is capable to angulate the needle. Angulated insertion would be useful for targets hidden by pubic bones and other critical structures. Once the safety of the system is confirmed through the study, we will extend its application to targets that require angulated needle insertion.

Acknowledgements. This work is supported by R01CA111288, P41EB015898, P41RR019703, U54EB005149 from NIH.

References. [1] Siegel R, et al. CA Cancer J Clin. 2014; 64(1):9-29. [2] Roehl KA, et al. J Urol 2002; 167(6):2435-2439. [3] Presti JC, Jr., et al. J Urol 2003;169(1):125-129. [4] Beyersdorff D, et al. Radiology 2002; 224(3):701-706. [5] Cormack RA, et al. Urology 2000; 56(4):663-664. [6] Susil RC, et al. J Urol 2006; 175(1):113-120. [7] Eslami S, et al, IEEE Int Conf Robot Autom 2013; 20132:1228-1233. [8] Gering, DT, et al, J Magn Reson Imaging 2001. 13(6): 967-75. [9] Fedorov A, et al. J Magn Reson Imaging 2012; 36(4):987-92. [10] Tokuda J, et al. Int J Med Robot 2009; 5(4): 423-34.



Figure 1. (A) The manipulator was docked on the patient table. (B) The needle was manually inserted by the radiologist in the 3T MRI scanner.

Evaluation of Breast Tissue with Confocal Strip Mosaicking Microscopy: a potential platform for rapid pathology to guide surgery

Sanjee Abeytunge^d, Gary Peterson^c, Ricardo Toledo-Crow^d, Monica Morrow^b, Melissa Murray^a, Milind Rajadhyaksha^c

^aBreast Pathology, ^bBreast Service, ^cDermatology Service, ^dResearch Engineering Laboratory, Memorial Sloan-Kettering Cancer Center, New York, NY, U.S.A

Purpose

Breast-conserving therapy (BCT), a combination of lumpectomy and radiation therapy, is the most common treatment for early stage breast cancer in the United States. Achieving negative margins is critical to BCT because positive margins increase rates of local recurrence. Histopathologic assessment of the lumpectomy margins typically takes a minimum of 2-3 days. There is a clear benefit to knowing if a margin is positive at the time of initial surgery to allow re-excision to be performed during the same operation, avoiding the cost and morbidity of a subsequent operation. Current rates of re-excision after BCT vary widely in single institution studies, ranging up to 70%. There is an unmet need for a technique which would allow adequate intraoperative surgical margin assessment.

Methods

In an IRB approved study, 74 fresh breast tissue samples from 39 patients were imaged within ten minutes of excision using a method called confocal strip-mosaicking (CSM) microscopy. Following CSM images were collected: 19 invasive ductal carcinomas (IDC), 18 ductal carcinoma in situ (DCIS), and 37 benign breast specimens which included fibroadipose tissue, mammary ducts and lobules, and fibrocystic changes. The fresh tissue specimens were immersed in 0.6 mM acridine orange (AO) for 45 seconds and imaged with the CSM microscope. CSM microscope produces strips of images – 0.5 mm wide with 2- μ m lateral resolution and 10- μ m optical sectioning - of the entire specimen. The strip images were merged (stitched) along the length of the strip to create a mosaic. 2cm x 2cm breast tissue samples were scanned under five minutes. Two mosaics were acquired in two modes of contrast: fluorescence highlighting the nuclei, and reflectance highlighting the stroma. The mosaics are digitally colored in blue (fluorescence) and pink (reflectance) to simulate the appearance of H&E histology. Specimens were subsequently processed in routine H&E histology sections and compared with CSM mosaics by our pathologist.

Results

Features such as invasive ductal carcinoma are identified in the CSM images and correlate well with the histopathology. The size and shape of the invasive tumor match the histopathology, and the interface of the invasive carcinoma and surrounding adipose tissue can be accurately outlined. DCIS can be detected where dilated ducts are expanded by proliferation of cells. Fibrous stroma can be distinguished from surrounding adipose. Adipocytes are visualized as round or oval with individual well-circumscribed cell borders. Breast lobular units are visible as a cluster of glands and ducts were visible as round structures within the fibrous stroma.

Conclusions

Strip mosaicking confocal microscopy offers an imaging technology platform for real time detection of tumor margins directly in fresh tissue during surgery and from biopsies. Large amounts of tissue may be examined for tumor margins rapidly enough to be of practical use in surgical and clinical settings. The imaging can potentially be developed into an adjunct for pathology, to enable more complete and accurate removal of tumor.

CT based Radiomics data predicts for nodal involvement and overall survival in NSCLC

T. Coroller¹, P. Grossmann¹, E. Rios Velazquez¹, R. Mak¹, H. Aerts¹

¹Brigham and Women's \ Dana Farber Cancer Center, Harvard Medical School, Boston, MA

Purpose: Recent advances in medical imaging technologies provide opportunities to quantify the tumor phenotype throughout the course of treatment non-invasively. The emerging field of “radiomics” addresses this by converting medical images into minable data using a large number of quantitative imaging algorithms. The ability of radiomics to predict clinical outcomes such as survival or nodal involvement can provide valuable complementary information. This study aims to evaluate the predictability of CT based radiomics features for node stages and survival time in non-small cell lung cancer (NSCLC) patients.

Method: We included 118 patients with NSCLC in our analysis. Seventy-four quantitative radiomic features describing the tumor phenotype based on intensity, shape, and texture were extracted from planning CT scans. Association of the radiomics features with node involvement (Yes/No) was assessed using the area under the curve (AUC) of the receiver operating characteristics (ROC). Association with overall survival was assessed using the C-Index (CI).

Results: We found 30 radiomic features that were significantly (FDR corrected) associated with nodal involvement (range AUC=0.73-0.60). Seventeen features were significantly associated with survival (range CI=0.56-0.62). Gray Level Non-Uniformity, describing intra-tumor heterogeneity, was the best predictor for both nodal stage (AUC=0.73) and survival time (CI=0.62). It is noteworthy that tumor volume is only the 8th best predictor for both nodal stage (AUC=0.71) and survival (CI =0.61).

Conclusion: Radiomics analysis was able to predict node stage and survival time by looking at complex image features. Although tumor volume has been routinely used to predict outcome, this study shows that radiomic features capturing detailed information of the tumor phenotype can provide better prediction for clinical relevant factors such as nodal involvement and survival.

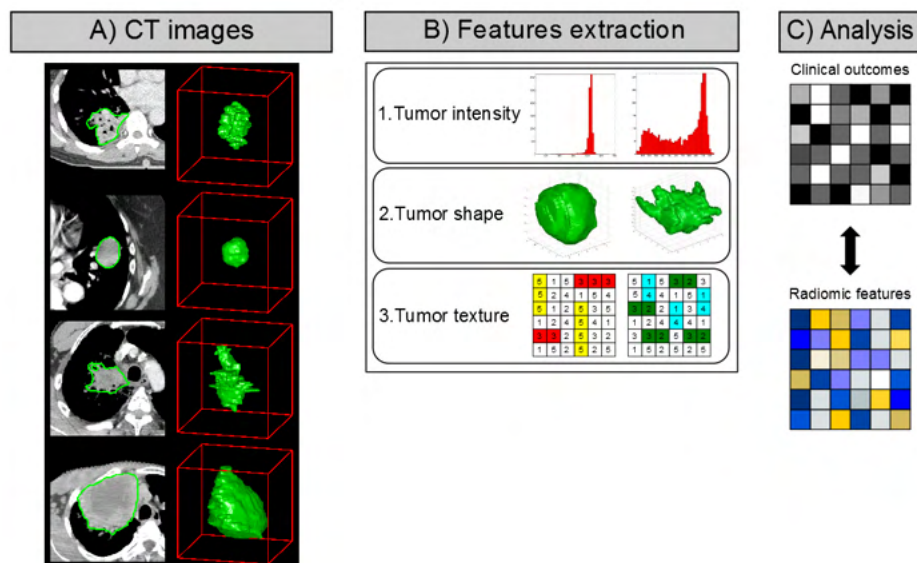


Figure: Radiomics workflow. To capture tumor phenotypic differences from CT images (A), we extracted radiomic features (B) including tumor intensity, shape and texture. Then, radiomics information are linked (C) to clinical data.

Comparative Study of Validation Metrics for Percutaneous Microwave Ablation against a 4D Thermal Simulation

Garron Deshazer*, Scott Collins**, Edward Walsh PhD***, Derek Merck PhD**, Damian Dupuy M.D.**

*University of Rhode Island, **Rhode Island Hospital, ***Brown University

Purpose. Image-guided percutaneous ablation is an effective, inexpensive, and accessible treatment for liver, lung, and kidney cancers. The relatively high recurrence rate of percutaneous ablation makes it usually palliative only. We hypothesize that the recurrence rate is due in part to an inaccurate, over-simplified treatment modeling and validation framework in procedure planning. We discuss using physically-based generative modeling with future opportunities for incorporating statistical uncertainty as an approach to predictive planning. Validation metrics for clinical and other experimental scenarios include visual inspection, 3D computed tomography (CT) imaging, 4D CT acquisition, and magnetic resonance (MR) thermographic mapping.

Methods. The proposed model uses finite element methods based on first principles to solve Penne's Heat Equation and Maxwell's equations for electromagnetic energy transfer in matter over time. Given electromagnetic, power dissipation, and heat boundary conditions for the solution domain, and inputs such as antenna composition and tissue properties, time-dependent physical partial differential solutions are found. The simulation for this experiment is based on a generic antenna inside homogeneous liver tissue with a generator setting of 60 watts for 15 minutes. Several different ablation margin validation approaches were taken to validate the simulation including visual inspection and CT data acquisition. To demonstrate relative temperature mapping, a MWA experiment with an agarose phantom was performed using MR thermal mapping technique. A simulation of the experiment was performed and fiber optic thermal couples were used as a baseline standard to evaluate the accuracy of the simulation and MR post-processing techniques to generate the thermal maps.

Results. The resultant isothermal contours of the time-dependent simulation indicated agreement of 0.2 cm when superimposed to the 4D CT images. This was under the assumption that all tissue inside the 45 degrees isotherm was a part of the ablation zone. The results of the coagulogram generated from the binary CT data of the ex-vivo bovine liver were within 0.35 cm agreement with the vendor specified ablation zone. 3D CT measurements when compared to visual inspection method were in disagreement by as much as 0.6 cm along the short axis of the excised tissue and as much as 0.5 cm along the long axis. The simulation of the agarose phantom showed a 5 degrees Celsius agreement when compared to the absolute temperature measurements with the thermocouples. The results of the MR thermal mapping showed after the ablation of the agarose phantom the MR relative temperature were within 1 degree Celsius

Conclusion. This initial model forms the basis of ongoing work in principled thermal simulation for ablation planning. Future goals are to incorporate heterogeneous tissue types and heat sinks into the solution domain, and validate the resulting simulation against our ongoing clinical data collection. In addition, creating an even more complex and possibly fused validation pipeline to evaluate simulation accuracy via 4D CT coupled with MR thermographic mapping would aid in understanding how the heat effect can be viewed and cell death be readily identified

Funding Source. Rhode Island Hospital, Diagnostic Imaging Department

Lung segmentation in 3D CT Images of Induced Acute Respiratory Distress Syndrome

Alfredo Morales Pinzón^{1,2}, Maciej Orkisz², Jean-Christophe Richard^{2,3}, Claude Guérin^{2,3}, and Marcela Hernández Hoyos¹

¹Systems and Computing Engineering Department, School of Engineering, Universidad de los Andes, Bogotá, Colombia

²Université de Lyon, CREATIS; CNRS UMR5220; Inserm U1044; INSA-Lyon; Université Lyon 1, France

³Service de Réanimation Médicale, Hôpital de la Croix Rousse, Hospices Civils de Lyon, Lyon, France

Purpose: Acute Respiratory Distress Syndrome (ARDS) has a mortality estimated between 40% and 50% in adults. Its management relies on mechanical ventilation to support the respiration. However, it is estimated that 25% of the deaths might be avoided with parameter setting of the ventilation better adapted to the particular patients. A study using an animal model (piglets) with ARDS induced, aims to analyze the response of the lung to mechanical ventilation. Computed Tomography (CT) images are used to quantify the aeration. This task requires the delineation of the lung in numerous images. However, in the case of ARDS, this delineation is hindered by the reduced contrast between lung and surrounding structures (see Fig. 1.C). The purpose of this work is to define a segmentation method that overcomes this difficulty.

Methods: The protocol requires the acquisition of one image in end-expiration and one in end-inspiration for different ventilation conditions. Each ventilation condition represents a combination of PEEP (Positive End Expiration Pressure) and Vt (Tidal Volume) of the mechanical ventilator. The method takes advantage of this protocol and consists of one initial automatic lung segmentation combined with a cascade registration and transformation process. (1) First, we obtain an initial lung segmentation (M_{pmax}) in the image that corresponds to the highest PEEP (I_{pmax}), which is the most contrasted image and its segmentation is the least challenging. (2) Then, a deformation field is calculated from a non-rigid registration of I_{pmax} to the image with the next highest PEEP (I_{pmax-1}). In this step, the registration uses a multiple B-spline transform that combined with the lung mask (M_{pmax}) preserves the sliding motion between the lung and the chest wall. (3) Next, the lung mask M_{pmax} is deformed to obtain M_{pmax-1} by using the deformation field found in the registration step. (4) Finally, steps (2) and (3) are executed in cascade using the next generation of images (I_{pmax-1} , M_{pmax-1} and I_{pmax-2}) until the last ventilation-condition image is reached.

Results: 584 images from 16 pigs were segmented and evaluated against manual annotations. As manual 3D delineation of the whole set of images is too demanding, 288 slices were contoured by an expert. These slices were randomly selected from groups representing different PEEP conditions, anatomical regions of the lung (i.e. top, middle and bottom), and respiration phases (i.e. end-inspiration and end-expiration) (Fig. 1). The average Dice similarity was 0.90 ± 0.17 for all the slices and 0.94 ± 0.04 , 0.95 ± 0.09 , and 0.80 ± 0.25 for top, middle and bottom slices, respectively.

Conclusions: The proposed method automatically segments the lungs in different mechanical ventilation conditions in an animal model with ARDS induced. The results present a high agreement with lung slices manually traced. Although the bottom region of the lung is the most affected by the low contrast, the method can achieve a high overlapping score.

Funding Sources: This work was performed within the framework of the LABEX PRIMES (ANR-11-LABX-0063) of Université de Lyon. Alfredo Morales Pinzón was supported by a Colciencias grant “Estudios de Doctorado en Colombia – 2011– Promoción 528”.

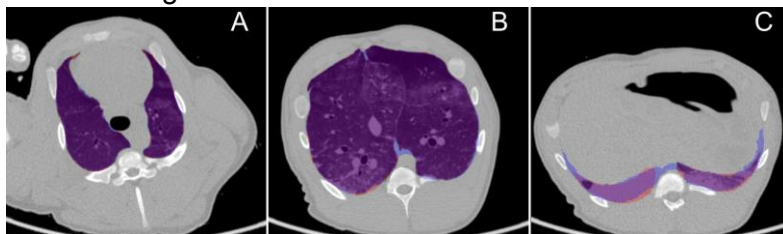


Figure 1. Example of axial slices of CT images with superposition of manual and automatic segmentations. (a) Top, (b) middle and (c) bottom slices of the lung. Manual and automatic segmentations are highlighted in orange and blue, respectively, while their intersection is highlighted in purple.

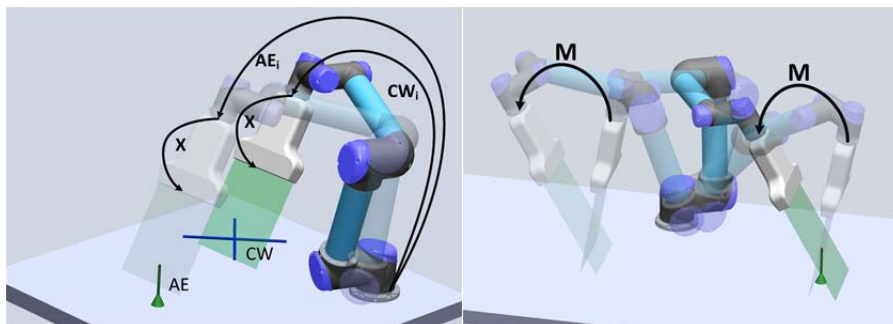
Advanced Approaches to Ultrasound Calibration: Planning a MICCAI Challenge

Emad M. Boctor (Johns Hopkins University, Baltimore, USA), **Kirby Vosburgh** (Brigham and Women's Hospital, Boston, USA), **Gabor Fichtinger** (Queen's University, Kingston, Canada)

The American Association of Physicists in Medicine (AAPM) Task Group #240 is generating a status report and recommendations for Ultrasound Guided Therapy. As a sub-task of this activity, led by Professor Boctor and the co-authors, we present a new approach to comparison of ultrasound calibration methods. The process for ultrasound calibration, particularly to enhance the robustness, real time accuracy, and applicability to challenging tasks such as registration to organs which have deformed or changed shape due to advances in disease, impacts of therapy, or changes in patient position.

Methods: We have developed a platform that can enable, for the first time, controlled comparative evaluation of different ultrasound calibration approaches. The authors propose to work with the attendees of this meeting on a MICCAI 2015 challenge using the data we are acquiring from this new platform. Ultrasound calibration recovers the unknown transformation from a rigidly attached tracked sensor to the ultrasound image. This process is necessary to enable advanced ultrasound-guided surgical interventions. There have been many ultrasound phantoms presented in literature. In general, they rely on some motion of the tracked ultrasound transducer. The field has lacked a way to robustly compare different calibration phantoms as it has been difficult to accurately reproduce the same motion for multiple phantoms. A robot arm provides a way for generating reproducible motions. It becomes possible to generate near-identical relative motions between multiple poses. For certain classes of phantoms (Z-wire, planar), these can be identical as any pose can produce a valid ultrasound image. For other classes of phantoms (point-based, crosswire, active echo), identical motions can only occur if the remote center of motion is the point as the point may be out of plane otherwise. Thus, identical orientations may be more practical. One can place multiple ultrasound calibration phantoms side by side and acquire ultrasound images of all of them using the same motions. One can also save a set of robot poses and use them to image multiple ultrasound calibration phantoms sequentially.

Results: The robot actuator design is shown in the figure. The phantoms are below the actuator system. The probe position and angle can be set precisely, and scan patterns replicated to directly compare phantoms of different types, as shown on the right.



Summary: A new robotics-based system for cross-comparing ultrasound calibration methods has been described and data is being taken. We will post data sets and the plan for next year's challenge. We look forward to your comments and participation.

Visit AMIGO on FRIDAY, September 19, 9am-4pm

Tours of the Advanced Multimodality Image Guided Operating (AMIGO) suite, located at Brigham and Women's Hospital, 75 Francis Street, Boston, will take place on Friday, September 19 between 9am and 4pm.



AMIGO is the clinical translational test-bed for research the National Center for Image-Guided Therapy (NCIGT) at Brigham and Women's Hospital (BWH) and Harvard Medical School. NCIGT and AMIGO are funded under the Biomedical Technology Resource Centers program of the National Institute of Biomedical Imaging and Bioengineering (P41EB015898, PI Jolesz, Tempany). A unique resource for Image-Guided therapy, AMIGO represents and encourages multidisciplinary cooperation and collaboration among teams of surgeons, interventional radiologists, imaging physicists, computer scientists, biomedical engineers, nurses and technologists to reach the common goal of delivering the safest and the most effective state-of-the-art therapy to patients in a technologically advanced and patient-friendly environment.

Launched in 2011, AMIGO is the first operating room-interventional suite facility with a full array of imaging modalities for use during procedures, enabling less invasive, more effective therapy. It covers a 5,700 square foot area divided into three sterile procedure rooms in which multidisciplinary teams treat patients using multiple imaging modalities. The central operating room of AMIGO, with its ceiling-mounted single plane angiographic x-ray machine, is flanked by a PET/CT room on one side and an MRI room on the other. Each room has a separate entrance to the control corridor and support spaces.

In the MRI room is a high-field (3 Tesla) wide-bore (70 cm) MRI scanner integrated with full OR-grade medical gases, MRI-compatible anesthesia delivery and monitoring system, and therapy delivery equipment. The MR scanner is mounted on the ceiling and can traverse on ceiling rails to a fully draped patient on the OR table, a typical scenario for brain tumor surgery. The central OR is equipped with MRI-

compatible anesthesia delivery and monitoring systems, a surgical microscope with near-infrared capability, surgical navigation systems that track handheld tools, a ceiling-mounted single plane angiographic x-ray system, and ultrasound imagers. A unique feature of AMIGO is the inclusion of PET in the surgical environment. The PET/CT scanner is stationary and fixed to the floor. There is a shuttle system for transferring patients between the PET/CT table for imaging and the OR table for surgery.

Over 200 patients per year are being diagnosed or treated in AMIGO for diseases of the brain, spine, thyroid, lungs, breast, liver, kidney, prostate, and cervix.

616 Procedures in AMIGO 08/31/2011-09/05/2014

Neuro 124

- 82 Craniotomies/Biopsies
- 22 Transsphenoidals
- 11 Deep Brain Stimulation electrodes placement
- 7 Laser Ablations
- 1 Epilepsy Electrode Placement
- 1 Skull Base

Head and Neck 7

- 5 Parathyroidectomies/Hemithyroidectomies
- 2 MR Guided Soft Tissue Neck

Skeletal 3

- 1 MR Cryoablation/Biopsy (Spinal Tumor Mass)
- 1 MR Biopsy (Femur)
- 1 Biopsy PET/CT guided (spine)

Thorax 58

- 22 Video Assisted Thoracoscopic surgeries (iVats)
- 10 Breast Lumpectomies
- 8 Biopsy PET/CT guided (lung)
- 7 EP Cardiac Ablations
- 7 Microwave ablations PET/CT guided (lung)
- 3 Cryoablations PET/CT guided (lung, rib)
- 1 Cryoablation MR guided (paraspinal met)

Abdomen 188

- 114 Cryoablations MRI guided (liver, kidney)
- 27 Biopsies MR guided (liver, kidney)
- 18 Cryoablations PET/CT guided (liver, kidney)
- 16 Microwave Ablations PET/CT guided (liver, kidney)
- 9 Cryoablations & Biopsies MR guided (liver, kidney)
- 3 FDG PET/CT Guided Interventions (Liver)
- 1 Cryoablation & Biopsy PET/CT guided (liver)

Pelvis 236

- 147 Prostate Biopsies
- 73 Gynecologic Cancer Brachytherapy
- 7 Prostate Brachytherapy
- 5 Cryoablations MR guided (iliac, prostate)
- 1 Biopsy MR guided (penile)
- 1 Biopsy/Cryoablation combo MR guided
- 1 Biopsy PET/CT Guided (penile)
- 1 Cryoablation PET/CT Guided (pelvic tumor)

